ChemElectroChem

Chemistry Europe
European Chemical Societies Publishing
ChemElectroChem

RESEARCH ARTICLE OPEN ACCESS

Interfacial Atomic and Electronic Structures of LSM/YSZ Thin Films as Models for SOC Air Electrodes

Hebatallah Ali[1,2,3] | Patricia König[4] | Xuan Quy Tran[1,5] | Anton Kaus[6] | Hanna Türk[4,7] | Adnan Hammud[1] | Zahra Gheisari[1] | Vaibhav Vibhu[2] | Vladimir Roddatis[8] | Franz-Philipp Schmidt[1] | Raoul Blume[1,9] | Patrick Zeller[1,10] | Till Frömling[2] | Felix Gunkel[6] | Axel Knop-Gericke[1,9] | Karsten Reuter[4] | Rüdiger-A. Eichel[2,11] | Christoph Scheurer[4] | Thomas Lunkenbein[1,12,13]

[1]Abteilung Anorganische Chemie, Fritz-Haber-Institut der Max-Planck-Gesellschaft, Berlin, Germany | [2]Fundamental Electrochemistry (IET-1), Institute of Energy Technologies (IET), Forschungszentrum Jülich GmbH, Jülich, Germany | [3]Women Faculty for Art, Science and Education, Ain Shams University, Cairo, Egypt | [4]Abteilung Theorie, Fritz-Haber-Institut der Max-Planck-Gesellschaft, Berlin, Germany | [5]Institute of Nanotechnology, Karlsruhe Institute of Technology, Eggenstein-Leopoldshafen, Germany | [6]Peter Grünberg Institute 7 (PGI-7), Forschungszentrum Jülich GmbH, Jülich, Germany | [7]Laboratory of Computational Science and Modeling, IMX École Polytechnique Fédérale de Lausanne, Lausanne, Switzerland | [8]Interface Geochemistry Section, GFZ Helmholtz Centre for Geoscience, Potsdam, Germany | [9]Department of Heterogeneous Reactions, Max Planck Institute for Chemical Energy Conversion, Mülheim an der Ruhr, Germany | [10]Chemical Energy Department, Helmholtz-Zentrum Berlin für Materialien and Energie GmbH, BESSY II, Berlin, Germany | [11]Institute of Physical Chemistry, RWTH Aachen University, Aachen, Germany | [12]Bavarian Center for Battery Technology, University of Bayreuth, Bayreuth, Germany | [13]Chair for Operando-Analytics for Electrochemical Energy Storage, University of Bayreuth, Bayreuth, Germany

Correspondence: Christoph Scheurer (scheurer@fhi.mpg.de) | Thomas Lunkenbein (lunkenbein@fhi-berlin.mpg.de)

Received: 30 August 2025 | **Revised:** 15 November 2025 | **Accepted:** 27 November 2025

Keywords: atomic resolution scanning transmission electron microscopy | complexion | lanthanum–strontium manganite thin films | solid oxide cells

ABSTRACT

Solid oxide cells (SOCs) are highly efficient electrochemical devices, yet their high-temperature operation induces structural instabilities that limit long-term performance. Thin-film electrodes provide a model platform to probe such effects due to their well-defined geometry and chemistry. Here, we combine high-resolution electron microscopy, synchrotron X-ray spectroscopy, and density functional theory to investigate the thermal stability of epitaxial lanthanum–strontium manganite (LSM) films on yttria-stabilized zirconia (YSZ). Comparing ultrathin (5 nm) and thick (200 nm) films under sintering (1150°C) and operating (800°C) conditions, we identify distinct degradation pathways: thick films remain largely stable but form interfacial $La_2Zr_2O_7$, while ultrathin films gradually dewet and aggregate, underscoring their instability as model electrodes. Furthermore, we show that the LSM bulk favors the less conductive rhombohedral phase, whereas, at the LSM/YSZ interface, a cubic-like LSM polymorph with enhanced electronic transport is stabilized, accompanied by oxygen vacancies, $Mn2^+$ enrichment, and cation disorder. These insights provide design principles for stabilizing interfaces to improve the efficiency and durability of SOCs.

1 | Introduction

Amid global efforts to decarbonize and transition the energy grid away from fossil fuels, green hydrogen is increasingly seen as a sustainable alternative fuel [1]. Meeting this growing demand requires technologies for hydrogen production that are both efficient and scalable. Solid oxide cells (SOCs) are particular promising in this context, offering high-efficiency energy conversion and the ability to utilize intermittent solar and wind energy [2, 3]. To unlock this potential, SOC materials must be optimized for both performance and long-term durability. A key aspect of this optimization is understanding the atomistic processes at the air electrode, where the oxygen evolution reaction (OER) occurs

Hebatallah Ali, Patricia König, and Xuan Quy Tran contributed equally to this work.

and deactivation processes have been reported in numerous studies [4–7].

The electron conducting air electrode consists usually of a perovskite (here lanthanum–strontium manganite, LSM) interfaced with a solid ion conducting electrolyte [6]. LSM belongs to an attractive class of transition-metal oxides, whose properties are wide-ranging from colossal magnetoresistance for spintronics [8] over a high Curie temperature for magnetocaloric energy conversion [9] to significant electronic conductivity and chemical stability rendering them suitable as air electrode material for high-temperature SOCs [10]. Additional control of LSM properties may be achieved by compositional variation [11], morphology adaption from bulk over thin films [12–14] to nanoparticles [15], or interfacial coupling with other complex oxides [16–19]. This could give rise to an unconventional behavior of local structures which significantly impact the underlying electronic [11] and magnetic properties [15, 16, 19], or catalytic activities [12–14].

In the context of SOC applications, electrodes based on LSM thin films have attracted considerable attention [20–24] owing to their well-defined geometry, morphology, and composition [20]. This stands in contrast to conventional porous electrodes, where the microstructure is more complex and strongly dependent on the specific fabrication processes [20]. The simpler structure of thin films compared to bulk material enables its controlled studies as a model SOC electrode, enabling valuable insights into reaction pathways and structure–property relationships in SOCs. Further advantages include the reduced influence of Ohmic losses as well as the possibility of employing it as a reference electrode for more precise measurements [20]. Beyond these aspects, the electronic conductivity of LSM has been the subject of significant experimental and theoretical investigation. Density functional theory (DFT) calculations, alternating-current (AC) and direct-current (DC) conductivity measurements have revealed that electronic transport in LSM involves charge carriers with a pronounced localized (polaronic) character [25, 26]. On the atomic scale, substitution of $La3^+$ ions by $Sr2^+$ introduces hole states, altering the $Mn4^+$ to $Mn3^+$ ratio and thereby modifying the electronic and structural environment of the Mn—O sublattice [27, 28]. This substitution gives rise to Coulombic inhomogeneities, Jahn–Teller lattice distortions [27, 29], and spin disorder [29], all of which contribute to complex polaronic behavior. As a result, different conduction regimes have been proposed, ranging from non-overlapping small polaron tunneling, through variable-range hopping, to overlapping large polaron transport [25, 26, 28, 29]. In particular, thermally activated small-polaron hopping and variable-range hopping are regarded as dominant mechanisms for charge transport at high temperatures [25, 28, 29].

On the nano and atomic scale, the introduction of structural defects in nanocrystalline thin films of LSM has been explored with various resulting effects. For instance, a pure strain condition imposed on the LSM film by an underlying substrate has been shown to reduce the surface exchange kinetics of oxygen [30], which is additionally dependent on the film growth orientation [22]. Conversely, enhanced oxygen exchange and transport has been found in the presence of nanostructured grain boundaries [12–14] or dislocations [31], and the grain boundary resistance is reported to be negligible at the high operating temperatures [32]. The heterostructure interfaces formed between LSM and other oxides also exhibit intriguing functional properties, which potentially opens up a new design space to tune the magnetic and electronic properties by interfacial coupling of the oxygen octahedral rotations at the unit cell level [16].

A prominent example is the interface between the electron-conducting electrode LSM and the oxygen-conducting electrolyte, typically ceramic yttria-stabilized zirconia (YSZ), which is generally regarded as the active phase for the oxygen reduction reaction (fuel cell) or OER (electrolysis cell). The exact chemical fingerprint of the reaction site is unknown, but expected to take place at the triple phase boundary (TPB) between LSM, YSZ, and the gas phase [5–7]. In catalytic applications of SOCs where the sintering temperatures during cell fabrication as well as operating temperatures are typically significantly above 600°C, such an interfacial structure would be additionally promoted by a strong interdiffusion of cations, resulting in a self-limited complexion layer between LSM and YSZ [5]. This also involves the segregation of large Sr cations to the surface of LSM, forming SrO, $Sr(OH)_2$, or $SrCO_3$, whose stability depends on the ambient atmosphere and temperature, and which collectively have an adverse effect on the catalytic performance [6, 33, 34]. Furthermore, excess amounts of La/Sr in LSM can lead to the formation of resistive secondary phases such as $La_2Zr_2O_7$ (Fd-3m) [35, 36] or $SrZrO_3$, which are detrimental to the oxygen diffusivity at the LSM/YSZ interfaces.

In this work, we present a systematic investigation of the thermal stability and the structural evolution of a model SOC electrode, $La_{0.8}Sr_{0.2}MnO_{3-\delta}$ LSM thin films deposited on YSZ(001) single crystals (ZrO_2) doped with 8 mol% (Y_2O_3) by pulsed laser deposition (PLD). The LSM/YSZ thin-film model system was intentionally developed as a simplified, and precisely defined reference architecture, designed to facilitate systematic atomic-scale and electronic-structure investigations while remaining directly comparable to bulk LSM electrodes in SOCs. The latter, owing to their complex morphology and heterogeneous interfaces, are often challenging to probe using spectroscopic and microscopic methodologies. Two representative film thicknesses—5 and 200 nm—were specifically selected to capture distinct interfacial regimes: the thinner (5 nm) film enables access to the porous morphology and triple-phase boundary regions, whereas the thicker (200 nm) film provides a continuous LSM coverage, allowing the study of a well-defined LSM/YSZ interface. Our study combines complementary methodologies, including advanced scanning transmission electron microscopy (STEM), X-ray photoelectron spectroscopy (XPS), X-ray absorption spectroscopy (XAS), DFT, and structural modeling of the interface with classical force fields to capture both microstructural and atomistic changes in the LSM film, at the LSM/gas and at the LSM/YSZ interfaces. The dual-thickness approach ensures that both nondestructive spectroscopic (XPS) and high-resolution microscopic (TEM) analyses can be correlated while accounting for their intrinsic methodological differences. While, this multimodal approach allows us to disentangle the roles of morphology, crystallographic orientation, oxygen vacancy density, and cation redistribution in dictating the conductivity and catalytic activity of the electrode material.

We show that film thickness plays a decisive role in the thermal stability of LSM, with dense 200 nm films remaining structurally robust under sintering, whereas ultrathin 5 nm films undergo pronounced aggregation and dewetting. XAS and XPS further provide direct insight into how oxygen partial pressure and

temperature affect the local electronic states, emphasizing the distinction between morphology-driven spectral changes and intrinsic electronic structure variations. At the atomic scale, STEM and electron energy-loss spectroscopy (EELS) reveal oxygen depletion and $Mn2^+$ enrichment at the electrode–electrolyte interface, while DFT calculations predict energetically a transition from rhombohedral bulk symmetry to cubic-like interfacial symmetry directly at the LSM/YSZ interface, accompanied by enhanced electronic conductivity. The suppression of MnO_6 octahedral rotations during the rhombohedral-to-cubic transition in the LSM interfacial layers, observed in STEM, is closely reproduced by our atomistic thin-film interface models, yielding excellent agreement between theory and experiment. Taken together, these findings establish a mechanistic picture in which interfacial lattice distortions, vacancy accumulation, and mixed band–polaronic transport govern the active-state conductivity of LSM. By bridging structural, spectroscopic, and theoretical perspectives, our results provide a comprehensive framework that advances the understanding of LSM as a model oxygen electrode material and offers critical benchmarks for its future *operando* investigation in SOCs.

2 | Results and Discussion

2.1 | Thermal Stability and Structural Evolution of LSM Thin Films at SOC-Relevant Temperatures

2.1.1 | Characterization of Pristine LSM ThinFilms

LSM films with nominal thicknesses of 5 and 200 nm on YSZ (001) substrates, namely, LSM-5 and LSM-200, respectively, were synthesized by PLD. In the plain view of the SEM (Scanning Electron Microscopy) images shown in Figure 1a,b, the pristine films display an interconnected network of granular LSM, which appears visually different from other studies using a different Si substrate [37] or different deposition techniques [38]. A survey of XPS spectra for these films, recorded in ultrahigh vacuum (UHV, 10^{-8} mbar) with 1400 eV photon energy, is also shown in

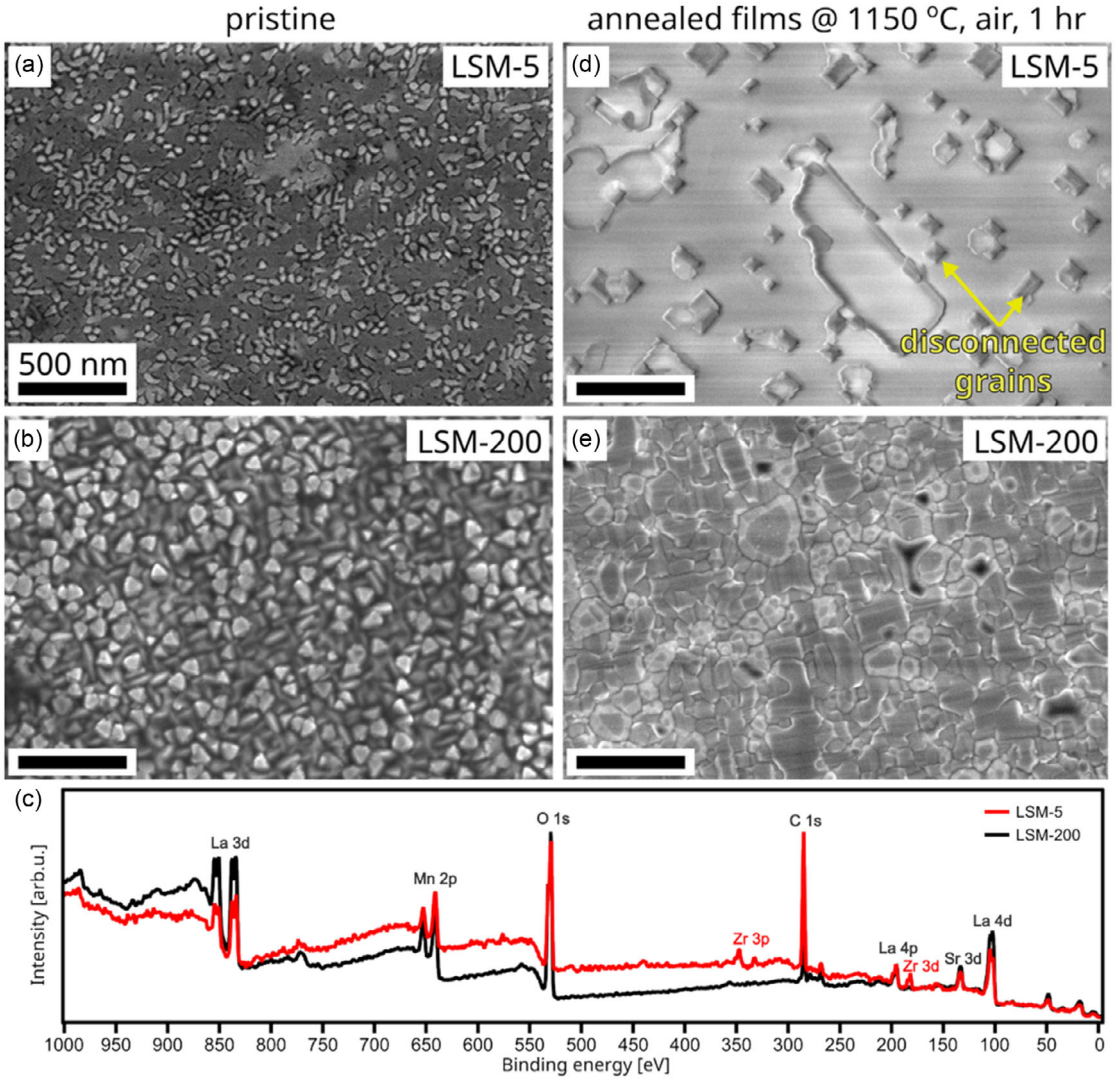

FIGURE 1 | Pristine LSM films and the effect of annealing at 1150°C in air for 1 h. Plan-view secondary electron SEM micrographs of the (a,d) LSM-5 and (b,e) LSM-200 films on YSZ substrates in the pristine and annealed states, respectively. The heating/cooling rates were 2°C/min. The micrographs were acquired under low voltages at 1.5 or 2 kV. (c) Survey XPS of the pristine LSM-5 and LSM-200 films measured at 1400 eV photon energy. The core-level contributions from La 3d, Mn 2p, O 1s, C 1s, La 4p, Sr 3d, La 4d, and the valence band orbitals are observed in both spectra.

Figure 1c. At this photon energy, the kinetic energy range varies from ≈550 eV for the La 3d orbital to around 1200 eV for the Zr 3d orbital. According to the universal curve for the inelastic mean free path [39], these kinetic energies correspond to an estimated information depth ranging from ≈0.9 to 2.4 nm beneath the sample surface. Both spectra display photoelectron signals from the La 3d, Mn 2p, O 1s, La 4p, C 1s, La 4p, Sr 3d, and La 4d core levels as well as the valence band orbitals. Notably, only in the LSM-5 film, additional signals stemming from Zr 3p and Zr 3d orbitals are detected. These signals are attributed to the porosity of the LSM layer and consequently photoelectrons emitted from the YSZ substrate can be detected. It should be noted that the spectra exhibit different background levels, which can be attributed to variations in carbon contamination species concentration between the LSM-5 and LSM-200 samples, as observed from the C1s peak intensities.

Furthermore, electron transparent lamellae were extracted from the thin film model systems using a focused ion beam (FIB). In line with the XPS data, the LSM-5 film is porous as characterized by voids between the nearby LSM domains of various heights (ca. 5–15 nm) (Figure S1). In contrast, the LSM-200 film is dense and exhibits a columnar texture along the growing direction (Figure S2). This observation is in agreement with the above SEM and XPS results. Moreover, both films are generally homogeneous in La, Mn, and Sr compositions based on energy dispersive X-ray spectroscopy (EDX) mapping in the STEM mode at the nano scale (Figure S1 and Figure S2).

2.1.2 | Annealing Effect at the Sintering Temperature 1150°C

The films were then subjected to various annealing steps to assess their thermal stability under relevant sintering and operating conditions of the bulk SOCs, which typically take place at 1000–1200°C (sintering) and at 700–900°C (operation). The sintering process is a critical step during the bulk SOC electrodes fabrication. It consists of annealing the electrode material at elevated temperatures, slightly below its melting point, in an air atmosphere to prevent liquefaction. This treatment reduces electrode porosity while simultaneously improving mechanical strength and ensuring structural stability under relevant operation conditions. In this study, the LSM thin film was annealed at 1150°C in air for 1 h. These sintering conditions have been reported to promote the formation of an interfacial layer (or complexion [5, 40]) within the bulk cells, which facilitates the diffusion of oxygen ions. However, significant changes to the film morphology were observed in the SEM micrographs of Figure 1d,e, especially for the LSM-5 film where a complete isolation of the agglomerated LSM grains was visible in addition to a severe elemental segregation (Figure S3). This is undesirable as a disconnected network of LSM would mean a loss of electrical percolation, making these isolated grains ineffective during the electrochemical operation of the cells. In contrast, the LSM-200 film still remained interconnected and compositionally stable despite the growth of the domain sizes (Figure S4). Furthermore, at such high annealing temperatures, nanoscale islands ($La_2Zr_2O_7$; space group: Fd-3m) have been occasionally observed at the LSM/YSZ interface of the annealed LSM-200 film (Figure S10 and Figure S11). This is also in agreement with previous studies [35, 36]. Such a secondary structure is undesirable as it impedes the electronic [41] and ionic conductivity [42], as well as leading to thermal expansion mismatches with the parent oxides [41]. Nevertheless, its contribution to the overall performance is deemed minimal due to its minor presence.

The main objective of applying the sintering treatment is to decrease porosity and thereby enhance the electrical conductivity and catalytic activity of the thin-film electrodes. However, under these annealing conditions optimized for bulk LSM electrodes, this aim could not be achieved. This is particularly clear in the case of thinner LSM films (LSM-5), which displayed variations in the film thickness and the morphological discontinuities. Such heterogeneity can significantly compress electrochemical catalytic performance of the LSM-5 thin-film electrode. Moreover, the appearance of secondary phases, observed for the LSM-200 film, most notably nanoscale ($La_2Zr_2O_7$; space group: Fd-3m) islands, must be strictly avoided, as their formation diminishes the catalytic effectiveness of the electrode–electrolyte interface. Accordingly, our subsequent annealing investigation is directed toward the behavior of the thinner LSM-5 films under realistic operating temperatures, while deliberately omitting the sintering step during fabrication. This focus arises from the demonstrated incompatibility of bulk-electrode sintering conditions with thin-film architectures, where such thermal treatments produce effects opposite to those reported for bulk cells. Establishing this distinction provides both the foundation and the motivation for a systematic investigation—presented in the following section—into the stability of LSM-5 thin films during annealing at operational temperatures.

2.1.3 | Annealing Effect at the Operation Temperature 800°C

In this section, we examine the effect of prolonged thermal treatment at 800°C, which is the typical operation temperature of an LSM electrode SOC, on the structural and chemical stability of the pristine LSM-5 film under atmospheric conditions. Figure 2 displays a series of secondary electron SEM micrographs: (**a**) the as-prepared film, and films annealed for (**b**) 1 h, (**c**) 12 h, and (**d**) 6 days. These images reveal the progressive morphological evolution of the film with increasing annealing duration. Initially, the LSM-5 film remains relatively intact up to 1 h of annealing. However, signs of grain aggregation and partial disconnection between neighboring LSM grains become evident after 12 h and are markedly pronounced after 6 days. This restructuring behavior is characteristic of solid-state dewetting—a well-known phenomenon in which thin films, metastable in their as-deposited state, undergo agglomeration at elevated temperatures to minimize surface energy [43, 44]. The dewetting and grain coarsening are also confirmed in the high-angle annular dark field (HAADF)–STEM images shown in Figure 2e,f, top tier, where the pristine and 6 day annealed films are compared. Notably, the latter exhibits larger LSM grains and increased spacing between them. Despite this significant morphological change, elemental analysis confirms that the LSM-5 film annealed for 6 days retains a homogeneous distribution of La, Mn, and Sr without noticeable phase separation or cation segregation (Figure 2e,f, bottom tier). Detailed EDX mapping of this sample is provided in the Supporting Information (Figure S12). Importantly, the observed dewetting behavior has direct implications for the functionality of LSM-based thin-film electrodes in SOC applications. As the film dewets, isolated regions become electrically disconnected and thus electrochemically inactive,

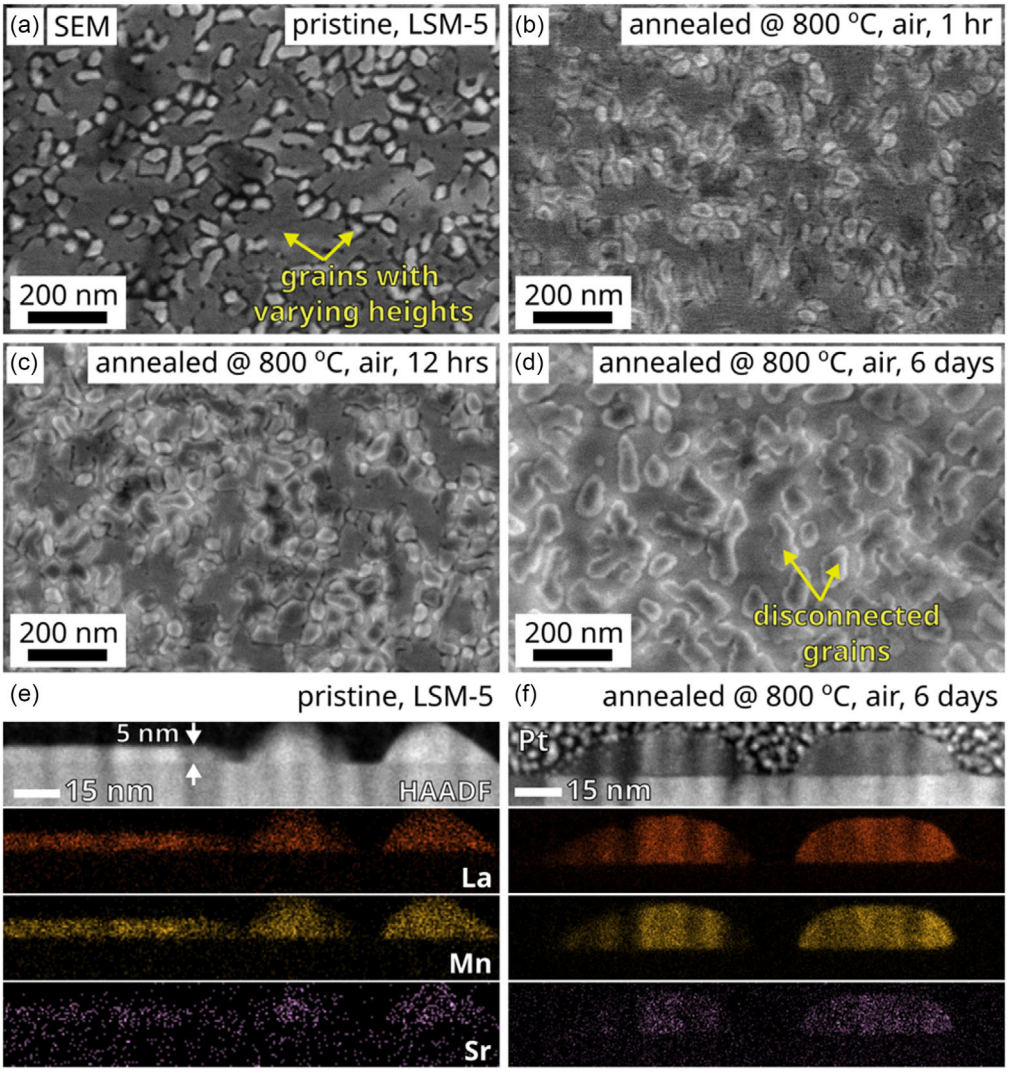

FIGURE 2 | Effect of annealing time (800°C, air) on the LSM-5 films. (a–d) Plan view secondary electron SEM micrographs of the LSM-5 film on an YSZ substrate ex situ annealed at 800°C for (a) pristine, (b) 1 h, (c) 12 h, and (d) 6 days, respectively. The heating/cooling rates were 2°C/min. The micrographs were acquired under low voltages at 1.5 or 2 kV. (e,f) Comparative HAADF–STEM images and EDX maps for the pristine and 6 days annealed film, respectively, from the cross-sectional views of the electron transparent lamellae. The elemental maps correspond to La L, Mn K, and Sr K lines. Further details can be found in Section S1 and Section S5.

potentially inducing local potential differences across the electrode and impairing overall performance. To further explore these morphological effects and their influence on the electronic structure, we conducted a combined Auger electron yield XAS (AEY-XAS) and X-ray photoelectron spectroscopy (XPS) investigation. XPS and AEY-XAS provide complementary insights into the electronic and chemical properties of the LSM surface: XPS reveals elemental composition and oxidation states, whereas, AEY-XAS provides information on the unoccupied electronic states and local coordination environment of the cations. Together, these techniques enable a comprehensive picture of the electronic structure evolution in the LSM films. These results are presented in Figure 3 and Figure S6, respectively.

Figure 3 displays the O K-edge and Mn L-edge X-ray absorption spectra (XAS) of the LSM-5 film, acquired by integrating the Auger electron yield (AEY) as a function of incident photon energy (commonly referred to as AEY-XAS). Measurements were performed on the pristine sample and after ex situ annealing in air at 800°C for 1 and 12 h (same samples imaged by SEM in Figure 2a–c). The O K-edge spectrum of both the pristine (black curve) and the 1 h annealed (green curve) LSM-5 samples appear nearly identical, indicating no thermal derived changes at this early stage. Generally, the features observed in the O K-edge XAS are associated with transitions from the O 1s to O 2p states, hybridized with Mn 3d orbitals—producing peaks labeled ***a*** (t_{2g}) and ***b*** (e_g). Additional features, peaks ***c*** and ***d***, originate from O 2p hybridization with La 5d and Sr 3d orbitals, while peak ***e*** is attributed to transitions involving Mn 4sp states [45]. Due to the porous nature of the LSM-5 thin film, AEY signals from the underlying YSZ substrate contribute to all the measured spectra. This contribution becomes more pronounced as film dewetting increases with annealing time, creating voids that allow more photoelectrons from the substrate to escape and be detected. After 12 h of annealing in air (red curve), the O K-edge spectrum shows significant changes at features ***a***, ***b***, ***c***, ***d***, and ***e***, indicating substantial modifications in the film. To further investigate the origin of the spectral changes observed in the O K-edge XAS, the corresponding Mn L-edges XAS spectra are presented in the right

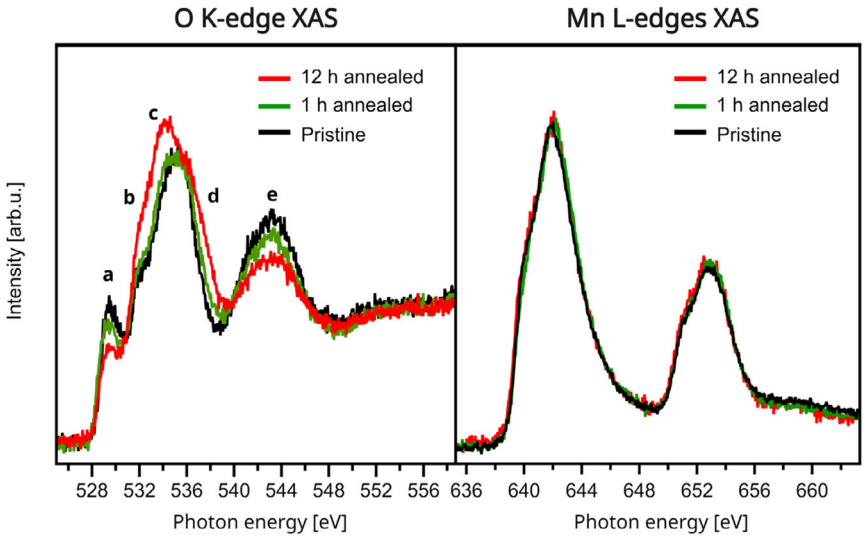

FIGURE 3 | O K-edge and Mn L-edges XAS spectra of LSM-5 thin films ex situ annealed at 800°C in air for 1-h and 12-h. The left panel shows the O K-edge XAS, highlighting the increasing relative contribution of the YSZ substrate signal due to morphological changes (e.g., dewetting) in the LSM film with extended annealing. The right panel presents the Mn L-edges XAS spectra, confirming that the local electronic structure of Mn remains unchanged throughout the annealing process.

panel of Figure 3. These spectra reflect electronic transitions from the Mn 2p orbitals to unoccupied Mn 3d states. Specifically, transitions from the Mn $2p_{1/2}$ level to the 3d t_{2g} and e_g orbitals appear at ≈640 and 642 eV (L_2-edge), while transitions from the $2p_{3/2}$ level to the same 3d suborbitals occur at around 651 and 653 eV (L_3-edge). The Mn L-edges spectra for the pristine, 1 h annealed, and 12 h annealed LSM-5 samples are almost identical. This consistency confirms that the elemental composition and Mn electronic structure remain stable throughout the annealing process. Complementary XPS analysis of the Sr 3d, Mn 2p, and La 3d core levels—measured from both the surface and the subsurface regions of the samples, corroborating the chemical stability of the LSM-5 film. These XPS measurements were performed on pristine, 1 h, and 12 h annealed samples ex situ after treatment at 800°C in air. The results, shown and discussed in Figure S8, substantiate the absence of significant surface segregation or compositional changes during prolonged thermal exposure. Consequently, the changes observed in the O K-edge spectra of the 12 h annealed sample are not attributed to modifications in Mn oxidation state or stoichiometry, but rather to morphological transformations within the thin film, as previously revealed by SEM imaging in Figure 2. In particular, dewetting and grain aggregation during prolonged annealing likely lead to increased porosity, exposing more of the underlying YSZ substrate. This enhances the relative contribution of substrate-derived signals in the AEY detection mode, thereby altering the overall shape and intensity of the recorded O K-edge spectrum. The differences observed are therefore a result of geometric and morphological evolution of the LSM film, rather than intrinsic electronic changes. Furthermore, the spectral difference between the 12 h annealed sample and the pristine sample is provided in the Section S5, as well as for comparison, a reference O K-edge spectrum of 10 mol% YSZ, adapted from the literature [46].

To mitigate the dewetting of the LSM-5 thin film during prolonged annealing, we reduced the oxygen partial pressure during the thermal treatment. This approach is well-documented in the literature, as oxygen pressure is known to influence thin film morphology, as well as the rate and mechanism of the dewetting process [47]. Understanding and controlling this parameter is essential for tailoring film stability and achieving desired morphologies for specific applications. To investigate this effect, an LSM-5 film was annealed in situ in the XPS chamber at 800°C under a reduced oxygen pressure of 0.5 mbar O_2 for up to 24 h. During this period, XPS and XAS measurements were continuously performed to track any changes in elemental composition, oxidation states, electronic structure, chemical bonding, or morphological evolution. Figure S8 shows the core-level XPS spectra of Sr 3d, Mn 2p, and La 3d, recorded every 6 h at fixed photoelectron kinetic energies of 150 and 950 eV. These kinetic energies provide surface and subsurface sensitivity, respectively, and allow for direct comparison with ex situ spectra acquired under UHV conditions (Figure S6). Notably, slight spectral differences arise due to oxygen gas adsorption on the LSM surface in the low-pressure annealing environment. In particular, the surface-sensitive Sr 3d spectra exhibit a slightly different shape compared to the subsurface spectra, which is consistent with earlier studies [6, 48]. A detailed peak fitting analysis of the Sr 3d spectra is presented in Figure S9, revealing a higher relative contribution of surface Sr species in the low kinetic energy measurements, while more bulk-like Sr signals dominate the higher kinetic energy spectra. This depth-dependent distribution aligns with established models of surface vs. bulk strontium segregation behavior under oxidizing conditions. Importantly, no significant spectral changes were observed throughout the 24 h annealing period, indicating stable elemental composition and oxidation states (Figure S6). This is further supported by the O K-edge and Mn L-edges XAS spectra (Figure S7), which likewise remained unchanged. It is also noteworthy that the shape of the O K-edge XAS spectrum under in situ conditions differs slightly from the ex situ spectra shown in Figure 3, due to additional contributions from gaseous O_2 in the chamber, which attenuate the XA-signals at 531 eV photon energy corresponding to the resonant energy of π^* orbital of molecular O_2. These findings demonstrate that lowering the oxygen pressure during

annealing effectively suppresses morphological dewetting in the LSM-5 thin film. This controlled environment also establishes a stable baseline condition for future electrochemical application evolving LSM-5 as a functional electrode material.

The results indicate that the thick, dense LSM-200 film remains thermally stable up to 1150°C, where the closely packed domains effectively suppress film aggregation. However, this stability is accompanied by the formation of secondary $La_2Zr_2O_7$ nanostructures at the LSM/YSZ interface. In contrast, the thinner porous LSM-5 film exhibits pronounced susceptibility to solid-state dewetting [43], most severe at 1150°C and still evident at 800°C. These findings suggest that ensuring sufficient film thickness is crucial for extending the lifetime of SOC components such as the air electrode, or a controlling gas pressure when thinner electrode films are necessary. While the porous morphology of LSM-5 film enables direct gas access at the LSM/YSZ interface, where triple-phase boundaries are formed, this advantage can be partially balanced in denser LSM-200 films by the presence of nanostructured grain boundaries, which may provide an alternative contribution for oxygen transportation. Indeed, previous studies have demonstrated that LSM grain boundaries exhibit mixed ionic–electronic conductivity [12–14], enabling oxygen ion transport toward the open surface where OERs occur. Nevertheless, a detailed understanding of oxygen dissociation, adsorption, and diffusion in LSM electrodes requires systematic investigation of the crystal structure orientation and its impact on both the gas–electrode and electrode–electrolyte interfaces. Accordingly, the following sections focus on the crystallographic properties of LSM, their influence on the electronic structure within the electrode bulk, and the resulting implications for gas interactions and interfacial processes at the LSM/YSZ boundary.

2.2 | Crystallography of LSM and Its Effect on the Electronic Structure

For SOC applications, the lanthanum manganite is typically doped with Sr^{2+} substituting La^{3+} cations at the perovskite A-site resulting in LSM, with a Sr/(La+Sr) ratio of ~0.1–0.2. This substitution enhances the electronic conductivity of LSM [49] while preserving the mechanical and chemical compatibility with the YSZ electrolyte [10, 49, 50]. Moderate Sr doping minimizes the formation of zirconate phases [51] and mitigates Sr surface segregation at elevated operating temperatures.

With a nominal doping of Sr/(La+Sr) = 0.2 in our study, LSM is known to crystallize in the rhombohedral structure (space group: R-3c:H) under ambient condition [5, 52]. In Figure 4a, we confirm this structure for a pure bulk LSM pellet reference sample used in our previous work [5, 7] using annular bright-field (ABF-STEM) imaging acquired along the $[1\text{-}1\text{-}1]_{rh}$ direction. It is visible that the MnO_6 octahedra are slightly rotated clockwise and counterclockwise by ≈7° in an alternating manner, forming a zigzag pattern of the oxygen lattices. This effect also reflects in the horizontal displacements of the oxygen lattices by approximately ±0.2 Å with respect to the Mn positions as illustrated in Figure 4a. These characteristic features are thus demonstrated for the rhombohedral structure (Figure 4a, left inset), which would have been absent in their cubic counterpart (Figure 4a, right inset).

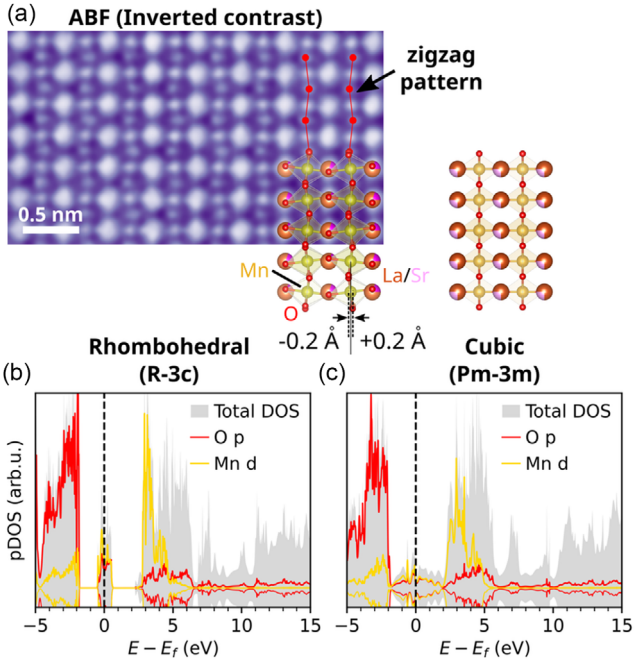

FIGURE 4 | Crystallography of the rhombohedral LSM and associated electronic structure. (a) ABF-STEM image (inverted contrast) of bulk LSM reference in a sintered pellet acquired along the $[1\text{-}1\text{-}1]_{rh}$ orientation. The alternating clockwise and counterclockwise rotations of the MnO_6 octahedra is characteristic of the rhombohedral structure (space group: R-3c:H) in the LSM, which is absent in its cubic counterpart (space group: Pm-3m). (b,c) Partial density of states (pDOS) calculated for the rhombohedral LSM and a hypothetical model of the cubic LSM, respectively. Both models share the same composition of $La_{0.83}Sr_{0.17}MnO_3$.

To further understand the influence of such a crystallographic feature on the electronic structure, we compare the DFT-derived partial density of states (pDOS) for two structure models (rhombohedral and cubic LSM) with and without the effect of MnO_6 octahedral rotation, respectively. With a selected composition of $La_{0.83}Sr_{0.17}MnO_3$ for both models, the rhombohedral LSM is more energetically favorable over the cubic counterpart at 0 K. In fact, the cubic LSM used in this case is only a hypothetical model for comparative purpose as a Sr/(La+Sr) content as high as >0.7 is usually required to stabilize this structure under ambient condition [52]. In LSM, Sr and La donate their electrons forming cations and the Mn 3d and O 2p orbitals form a hybridized state around the Fermi level which is responsible for most of the electronic conductivity in LSM [7, 53]. As seen from the pDOS for the rhombohedral LSM in Figure 4b, this hybridized state is localized at and around the Fermi level, and thus is responsible for the electronic conductivity in LSM [5]. However, there is a bandgap before and after the states near the Fermi level, this can impede an overall scattering of the electrons and decrease the electronic conductivity, since there is no continuous band transport possible. Interestingly, we find in the absence of the MnO_6 octahedral rotation, this hybridized state fills up the entire bandgap in the cubic LSM (Figure 4c), suggesting an improvement in electronic conductivity. On an atomistic level, this can be rationalized by the improved orbital overlap between the Mn 3d and O 2p orbitals in the nonrotated orientation which strengthens their hybridization and supports a more conductive band structure.

The atomic models, displayed in Figure 4b,c, are sourced from the ICSD [54] database and thus reflect the crystallographic average lattice with ideal cubic and rhombohedral positions, respectively. To get a more realistic understanding of the local MnO_6 octahedral motifs, we optimize the position of the atomic coordinates in dependence of their initial spin polarization states. The resulting potential energy landscape of LSM exhibits metastable and local minima depending on the proximity of the initial Mn spin moment to the differently charged Sr or La sites (see Figure S16). Finding the true global minimum for both the rotated and the nonrotated MnO_6 octahedral motifs requires initializing the full spin configurational space (see Table S1) and relaxing each configuration.

Relaxed cubic configurations without the octahedral rotation (Figures S17b and S18b) exhibit minimal distortion of the octahedral motif resulting in symmetric spin densities of the Mn-d-orbitals (see Figure S20) irrespective of the energetic location of the structure on the potential energy surface. The pDOS for those structures shows mostly symmetric bands between the spin up and spin down channels indicating that there is no directional preference for the spin transport in cubic MnO_6 arrangement [55].

In contrast, the relaxed rhombohedral structures (Figures S17a and S18a) show more pronounced (Jahn–Teller) distortions of the rotated MnO_6 octahedrons, giving rise to spin asymmetries and spin splitting around the Fermi energy (see Figure S19). More energetically stable structures show a higher degree of symmetry between the spin up and spin down channels in the pDOS.

We propose that these local lattice distortions, inherent to the rotated MnO_6 motifs in the rhombohedral cell, generate a continuum of spin-polarized states near the Fermi level, which is surrounded by state free regions. Therefore, the pure band conductivity character for our electrode material is inhibited. The spectrum of accessible states within the thermal energy range of $k_B \cdot T$, coupled with minor lattice distortions, facilitates the emergence of phonon modes that can stabilize polarons. The charge transfer mechanism in our anode material likely involves not only ideal band transport but also mixed conductivity, incorporating a polaronic hopping mechanism. This phenomenon has been previously reported for LSM [25–29]. Additionally, the spin splitting especially near the conduction and valence band edges in the pDOS opens the door for spin-selective electron transport and possibly plays a role in the adsorption process of molecular oxygen with unpaired electrons [55].

While these DFT calculations help to identify local structural motifs and provide valuable insights into the electronic behavior of bulk LSM, they rely—like most theoretical studies—on periodically infinitely often repeated small cells with fixed stoichiometry. At the LSM/YSZ interface, lattice symmetry is broken and the chemical environment becomes spatially heterogeneous [7]. To accurately capture the mechanisms governing charge transfer and reactivity at the interface, we have to go beyond an idealized bulk description and examine the atomistic structure and electronic properties of the interface itself. In the following section, we focus on constructing realistic interfacial models based on experimental observation.

2.3 | Atomic Structure at the LSM/YSZ Interface

To elucidate the atomic structure, we first examine structure characteristics of the experimentally investigated LSM/YSZ interface with STEM imaging, revealing various interface-related features such as a suppression of MnO_6 octahedral rotation, a localized accumulation of oxygen vacancies and dislocations, and a high degree of distorted cation lattices.

Due to the lattice mismatch between LSM and YSZ (ca. 6.9% as estimated from Figure S13), there exist several crystallographic variants of the LSM domains with respect to the YSZ (001) orientation (Figures S14 and S15). This also explains the columnar texture of the LSM-200 film and a large number of grain boundaries between the neighboring domains, which can be beneficial for oxygen ion transport [12–14]. The different orientations of the LSM domains seemingly influence the degree of lattice distortion at the LSM/YSZ interface and consequently, the effective thickness of the interfacial layer or complexion.

To gain an atomistic understanding of the interfacial structure, we selected an LSM domain of the annealed LSM-200 film (1150°C, air, 1 h) located in a region free from secondary-phase formation at the LSM/YSZ interface oriented along the LSM $[1\text{-}1\text{-}1]_{rh}$ direction with which we expect the change of oxygen lattices can be visualized as previously demonstrated in Figure 4a. The MnO_6 rotations from the rhombohedral LSM interface ressemble the rotations of the LSM bulk pellet in Figure 4. Figure 5 shows such a well-oriented LSM/YSZ interface along the $LSM[1\text{-}1\text{-}1]_{rh} \parallel YSZ[001]_c$ direction. While only metal cations can be seen in the low-angle annular dark-field (LAADF-STEM) image (Figure 5b), oxygen anions are additionally found in the corresponding ABF-STEM image (Figure 5a). On the LSM side, oxygen arrangement follows a zigzag pattern towards the interface; however, this pattern is sharply interrupted at the intermixed cation layer (Figure 5c) of the interface, resulting in an almost complete suppression of the MnO_6 octahedral rotation. In addition, a recurring array of oxygen vacancies ($V_o^{\bullet\bullet}$) is observed in the vicinity of this layer (red arrows in Figure 5).

To translate these experimental insights into atomistic models, we constructed interface models (see Figure S21) using crystallographic half-cells of LSM and YSZ with matched orientation, as observed in the microscopy data (Figure 5a,b). The models incorporated the same nominal doping as for our DFT bulk study on LSM $La_{0.83}Sr_{0.17}MnO_3$ and 8 mol% YSZ. A detailed description of the formation of the interface can be found in the Supporting Information. Notably, the YSZ annealed at 1150°C for 1 h exhibits close to the interface an array of oxygen vacancies, which is shown in Figure 5 (see red arrows). Upon structural relaxation, we observe a clear suppression of the MnO_6 octahedral rotation confined to the first few interfacial layers in the LSM region (see Figure S24 and S23), in excellent agreement with experimental observations. This indicates that lattice matching, local strain, and defect chemistry at the interface collectively stabilize a more cubic-like symmetry in LSM, distinct from the rotated octahedral configuration seen in the rhombohedral bulk structure. An overview of all accessible spin states and octahedral rotations in Figure S16 confirms that all cubic arrangements are energetically accessible from the most stable rhombohedral configuration by temperatures already as low as 800 K.

Normally, high-symmetry cubic LSM is only stabilized at high temperatures or with a high doping amount of Sr (Sr/(La+Sr) >0.7 [52]). However, it is noted that cations with large ionic sizes are less likely to be accommodated in this intermixed layer, which apply for the case of Sr from our previous finding [5].

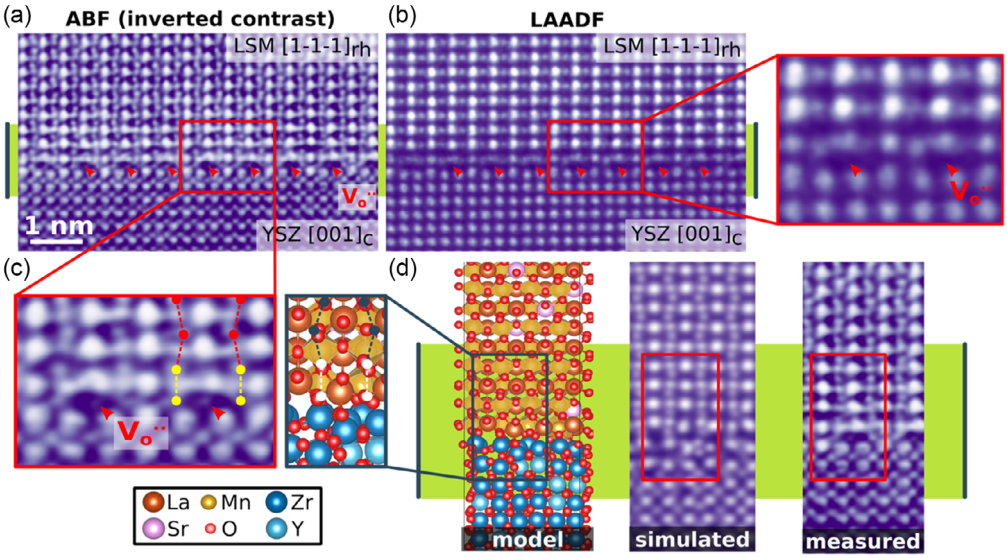

FIGURE 5 | Analysis of the LSM/YSZ interface by STEM imaging. (a,b) ABF- and LAADF-STEM images of the LSM/YSZ interface in an annealed LSM-200 film (1150°C, air, 1 h). (c) Zoom-in images corresponding to the insets in (a) and (d) a force field relaxed atomic model of the LSM/YSZ interface is used for illustrating the suppression of MnO_6 octahedral rotation and the presence of oxygen vacancies at the interfacial layer. For comparison, the simulated ABF and measured ABF images are displayed next to the model.

Therefore, the suppressed rotation of MnO_6 octahedra is probably linked to the constraint effect at the interface with the YSZ, and is predicted to enhance the electronic conductivity according to the pDOS result in Figure 4b,c due to continuous band states and fully degenerate spin channels which might enhance the OER activity in AFM as well [55]. Similar kinds of interfacial coupling of the oxygen octahedra across other complex oxides have been reported [56, 57], also giving rise to an increased electronic conductivity [56]. Bulk LSM is potentially a better polaronic conductor, since the complexity of various cationic site effects and defects at the interfacial region can lead to the breakdown of the conventional polaron hopping transport model [58]. The disordered systems very likely incorporate medium ranged sized polarons [29]. To fully understand the charge transport mechanism at the interface, further method advancement and simulations are required.

EELS line profile analysis was also used to probe the electronic structure of Mn across the same LSM/YSZ interface (Figure 6). The interfacial layer (ca. 1 nm) as seen from the ADF-STEM image in Figure 6a correspond to a sharp change of the compositional gradient for Mn $L_{3,2}$ and La $M_{5,4}$-edges across the LSM/YSZ interface in Figure 6b. This is highlighted by the green shaded zone in both Figure 6a,b. In addition, an increased concentration of $Mn2^+$ at the interface under the reducing condition of the electron beam is also evident by the peak shift and the increased Mn L_3/L_2 ratio compared to that of the bulk LSM (Figure 6c,d). This is in agreement with the localized accumulation of $V_o^{\bullet\bullet}$ at the interface observed previously in the ABF-STEM image (Figure 5). In other words, a lower oxidation state of Mn requires less oxygen for charge equilibration, hence more $V_o^{\bullet\bullet}$, which has also been reported at other oxide interfaces [61]. The observation of Mn(II) at the LSM/YSZ in these EELS measurements is due to local structural motifs which can energetically support fairly long-lived Mn(II) polaron species. These findings are in agreement with our previous study on bulk LSM/YSZ composite cells [7], demonstrating that despite the different fabrication routes, both systems exhibit comparable interfacial redox behavior characterized by Mn(II) enrichment confirming that these phenomena are intrinsic to the LSM/YSZ interface rather than an artifact of the thin-film geometry.

It is expected that the role of an interfacial layer is to mediate the lattice mismatch between the abutting LSM and YSZ phases (ca. 6.9% from Figure S13). This is often accompanied by the disturbance of metal cations within and neighboring to the interface [5]. To this end, a real-space approach involving Gaussian peak fitting of atomic columns and analysis of the local atomic positions was carried out on a drift-corrected LAADF-STEM image of the LSM/YSZ interface. This results in spatial contour maps of the projected interatomic distances between neighboring La/Sr cations denoted as *dx* and *dy* in Figure 7, which are overlaid onto the original LAADF-STEM image (Figure 7b,c). We find an alternating contraction and expansion of the interatomic distances *dy*, forming a chessboard pattern in the LSM region (Figure 7c). This behavior of *dy* is additionally reflected in the bimodal distribution in the corresponding histograms (Figure 7d). Such a behavior is intriguing as it would not have been expected for the rhombohedral structure.

In addition, at the LSM/YSZ interface, we find the local interatomic distances *dx* and *dy* contract/expand significantly beyond the average bulk values. Consequently, they appear as outlier values in the contour maps of Figure 7b,c and in the histogram distribution of Figure 7d. This is corroborated by a displacement vector analysis of the cation lattices presented in Figure 7e,f, which also reveals a high degree of lattice disturbances at the LSM/YSZ interface. Surprisingly, the magnitudes of atomic displacements diminish quite sharply away from the interface, most likely due to structure relaxation of the bulk LSM after high-temperature annealing [62]. This is consistent with our interfacial models, in which bulk-like properties re-emerge within just five to six layers from the interface. While strain in thin films has been regarded as detrimental to properties such as the electrical conductivity [63], the oxygen-vacancy diffusivity [64], and

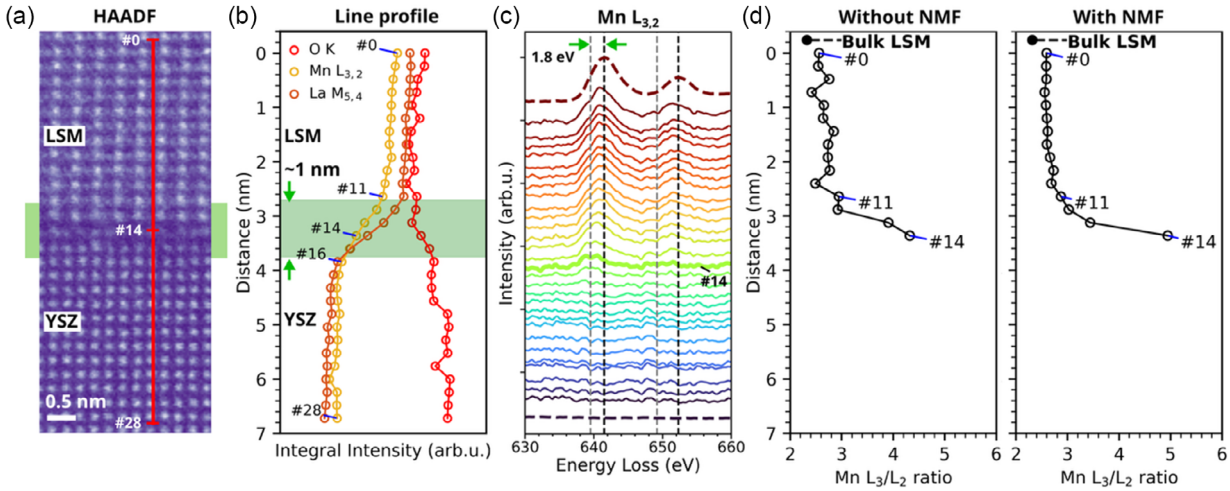

FIGURE 6 | EELS line profile across the LSM/YSZ interface of an annealed LSM-200 film (1150°C, air, 1 h). (a) HAADF–STEM survey image. (b) Integral intensity of O K-, Mn $L_{3,2}$-, La $M_{5,4}$-edges as a function of position across the LSM/YSZ interface, corresponding to the line profile indicated in (a). (c,d) Sequential series of Mn $L_{3,2}$-edge and the calculated Mn L_3/L_2 ratio, respectively, as a function of position across the LSM/YSZ interface. Additionally, a non-negative matrix factorization (NMF) process [59, 60] was used for the reduction of Gaussian and Poison noise in the spectra for the calculation of Mn L_3/L_2 ratio.

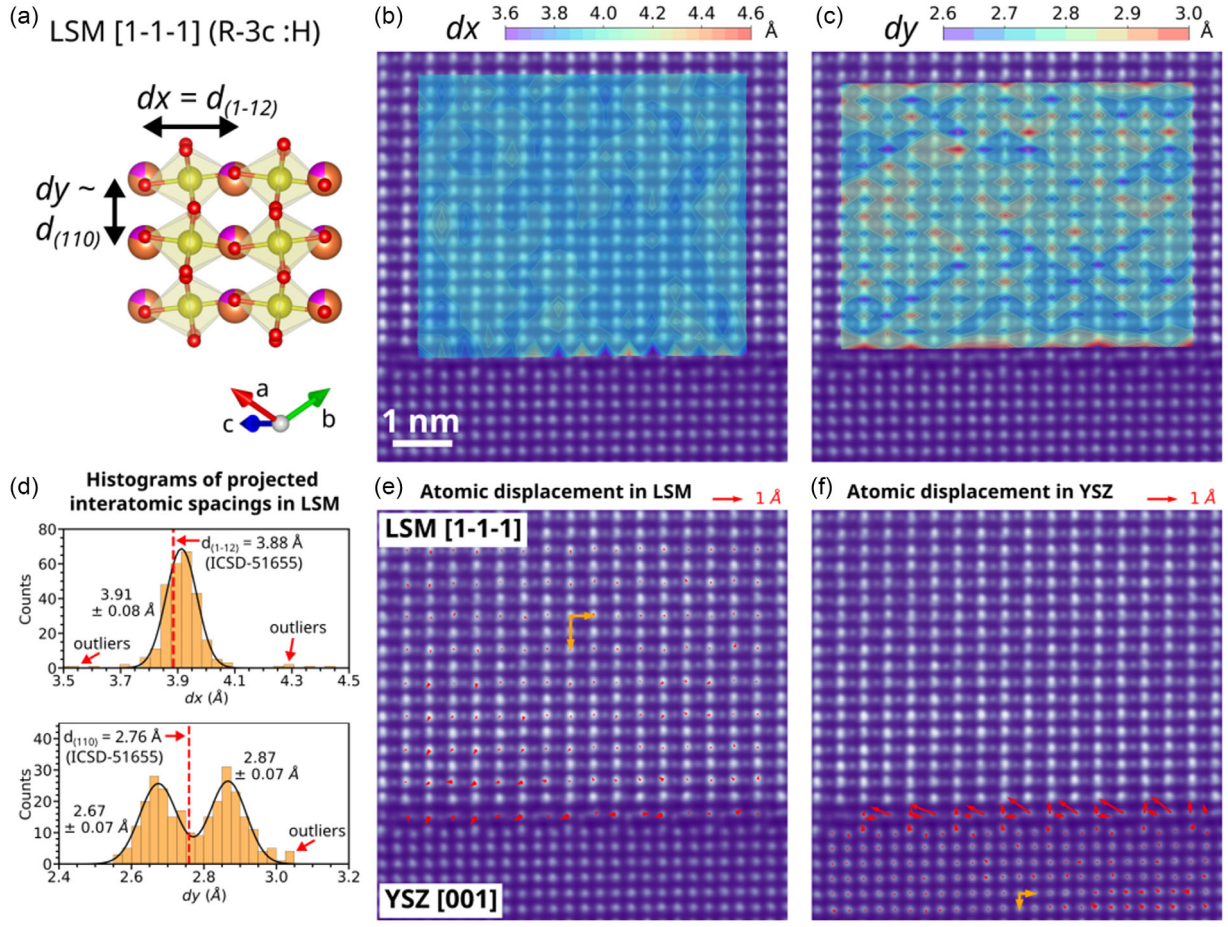

FIGURE 7 | Distortion of cation lattices near the LSM/YSZ interface of an annealed LSM-200 film (1150°C, air, 1 h). (a) Atomic model of the rhombohedral LSM viewed along the $[1\text{-}1\text{-}1]_{rh}$ direction in the hexagonal setting. (b,c) LAADF-STEM images of the LSM/YSZ interface overlayed by the contour maps of the projected interatomic spacing *dx* and *dy* in LSM, respectively, as denoted in (a). (d) Corresponding histograms of the projected interatomic spacing *dx* and *dy* in LSM. The mean values are compared to the referenced values of $La_{0.8}Sr_{0.2}MnO_3$ from the ICSD database (No. 51 655). (e,f) Atomic displacement maps of the La/Sr (LSM side) and Zr/Y (YSZ side) cation lattices, respectively. The orange axes define the origins of the reference lattices used for the calculation of displacement vectors.

surface oxygen exchange kinetics [30], it can also modulate metal–oxygen binding in ways that may enhance catalytic activity. The strain modulates the charge on the metal centers directly located at the interface and can alter the oxygen-metal binding, influencing adsorption, dissociation, and desorption of O_2. This introduces two competing effects: overly strong-binding prevents O—O dissociation, while overly weak binding limits oxygen adsorption.

From our present measurements, it is not yet possible to determine whether the combined effects of interfacial strain, suppressed MnO_6 octahedral rotations, and localized oxygen-vacancy accumulation enhance or hinder catalytic activity in the OER. Nevertheless, by elucidating the structural characteristics and local atomic environments in these thin films, we establish a robust platform for linking interfacial structure to catalytic function. This foundation will be essential for guiding operando studies and advanced simulations aimed at pinpointing the active catalytic sites and unraveling their dynamic evolution under reaction conditions.

3 | Conclusion and Outlook

In this work, we employed thin-film electrodes as simplified, well-defined model systems to investigate the behavior of LSM, a long-standing and widely studied oxygen electrode material for SOCs. The main objective was to address key open questions concerning the stability, efficiency, and catalytic pathways of LSM under fabrication and operational conditions. By systematically varying the film thickness and thermal treatment, we were able to disentangle the morphological, crystallographic, and electronic factors that govern the electrode performance at both the electrode bulk material, the electrode–gas and the electrode–electrolyte interfaces.

Two representative film thicknesses were chosen to capture contrasting morphologies and levels of accessibility to the TPB: a porous LSM-5 film and a dense LSM-200 film. Under sintering conditions (1150°C in air for 1 h), the LSM-200 film remained morphologically stable, though nanoscale $La_2Zr_2O_7$ was observed at the electrode–electrolyte interface. In contrast, the LSM-5 film underwent pronounced aggregation and dewetting, underscoring the susceptibility of ultrathin films to solid-state instability. Further investigations at operational conditions (800°C), in air, and in 0.5 mbar O_2 provided additional insight into how temperature, oxygen partial pressure, and gas environment influence the detected electronic structure. These variations were primarily correlated with morphological changes, as evidenced by XAS. Complementary X-ray photoelectron spectroscopy confirmed that the overall electronic structure remained stable. Together, these results highlight the importance of carefully distinguishing between morphological effects and genuine electronic structure changes when interpreting spectroscopic data. In particular, they demonstrate the unique value of combining XAS and XPS for probing the electronic structure of LSM electrodes, while cautioning against potential misinterpretations arising solely from morphology-driven signal variations.

The crystallographic analysis provided a deeper understanding of the link between structure and catalytic conductivity. Our films with a Sr/(La+Sr) ratio of 0.2 stabilized in a rhombohedral configuration, as confirmed by ABF-STEM imaging. Although this phase is energetically favorable, DFT calculations revealed that its electronic conductivity is reduced compared with the cubic phase. The rhombohedral distortion leads to increased electron scattering near the Fermi level, which interrupts band-like conduction and suppresses oxygen dissociation, adsorption, and diffusion processes. The analysis further indicated that charge transport in rhombohedral LSM may involve a mixed mechanism, combining limited band transport with polaronic hopping, thereby shifting the conventional picture of LSM conductivity.

Particular emphasis was placed on the LSM/YSZ interface, where striking structural and electronic modifications were observed. High-resolution STEM revealed a depletion of lattice oxygen accompanied by $Mn2^+$ enrichment, consistent with increased oxygen vacancy concentrations at the interface. DFT calculations supported these findings, predicting a cubic-like structure locally at the interface, in contrast to the rhombohedral bulk. This interfacial cubic symmetry was associated with more symmetric spin-up and spin-down states near the Fermi edge, indicating enhanced conductivity. Atomistic models constructed with classical force fields consistently reproduced the cubic symmetry motif observed in STEM at the interfacial LSM layers. Beyond the cubic symmetry directly at the interface, we observe variations in the cell arrangement and through systematic exploration of the parameter space for constructing these interfaces, we identify a range of possible interfacial structures, with the most promising candidates showing excellent agreement with experiment. These structures will serve for future studies to explore thermodynamical barriers and first-principles simulations of the electronic conductivity directly at the interface. EELS line profiles corroborated the enrichment of $Mn2^+$ and the accumulation of oxygen vacancies, while spatial mapping of cation displacements revealed strong lattice distortions confined to the interface, which gradually relaxed toward the bulk electrode. These results underline the complex interplay of crystal symmetry, oxygen vacancy dynamics, and electronic structure at functional interfaces—factors that critically impact SOC performance.

In conclusion, this study provides a comprehensive assessment of LSM thin films as model electrodes for SOCs. By correlating morphological stability, crystallographic orientation, interfacial structure at the atomic-scale, and electronic conductivity under both fabrication and operation-relevant conditions, we establish a detailed reference framework for future mechanistic investigations. Importantly, the findings demonstrate that while thin films offer simplified model systems, their behavior can diverge significantly from that of bulk electrodes, particularly under high-temperature treatments. Recognizing and understanding these differences is essential before extending insights to real device architectures. Our results form a crucial preparatory step toward *operando* characterization of LSM electrodes under electrochemical working conditions and more sophisticated electronic structure calculations of the thin film interface. The established structural and electronic benchmarks will guide the design of *operando* X-ray spectroscopy, as well as quasi in situ STEM experiments and the search for catalytically active structural motifs at the interface, aimed at capturing the dynamic processes of oxygen adsorption, dissociation, diffusion, and conduction as they occur during SOC operation. Ultimately, this approach will contribute to a more complete, multiscale understanding of LSM electrode functionality, enabling more rational design strategies for stable, efficient, and durable SOC electrodes.

4 | Experimental Section

4.1 | Thin Film Synthesis

LSM thin film samples were grown on (001) oriented YSZ substrates in a TSST PLD chamber with a KrF laser (λ = 248 nm). The substrates were annealed at 1350°C for 6 h before growth [65]. The thin films were deposited at 850°C under an oxygen partial pressure of 0.24 mbar [66]. The laser fluence was set to 2.9 J cm^{-2} and the distance between the ceramic target and the heated substrate was 55 mm. For the 200 nm LSM sample, the deposition was performed at a pulse repetition rate of 15 Hz, while 5 nm LSM samples were deposited at 5 Hz.

4.2 | Thin Film Annealing

The LSM-5 and LSM-200 thin films were annealed in an external ceramic furnace (model number ROC 50/250/14) with a heating rate of 2°C per minute. The samples were held at the target temperature (either 800 or 1150°C) for the specified duration, followed by controlled cooling to room temperature at a rate of 2°C per minute. All annealing treatments were conducted under ambient air at atmospheric pressure.

4.3 | Sample Preparation for Electron Microscopy

Electron-transparent lamellae containing the LSM/YSZ interfaces of the thin films were prepared with a Helios NanoLab G3 FIB-SEM DualBeam system (ThermoFisher Scientific, USA). The instrument is equipped with gallium ions having energies up to 30 keV. Additional polishing steps at low ion energies of 5 and 2 keV were used to minimize damage and redeposition of removed materials onto the lamellae's side walls.

4.4 | Electron Microscopy

Characterization of the nano and atomic structures was performed on a Cs-corrected JEM-ARM200F scanning transmission electron microscope (Jeol, Japan) under an accelerating voltage of 200 kV. Various STEM imaging modes were employed including bright field (BF-STEM), annular bright field (ABF-STEM), low-angle and high-angle annular dark field (LAADF-/HAADF–STEM). More specifically, ABF-STEM imaging was acquired on a BF detector with the inner/outer collection angles (8–18 mrad) limited by the beam stopper and a 3 mm bright field aperture, respectively. This method has been routinely used to detect light elements in the vicinity of heavy elements in crystalline materials [67–69]. The Gatan ADF detector angles corresponding to the HAADF and LAADF-STEM imaging modes are 53 mrad $< \theta <$ 118 mrad and 27 mrad $< \theta <$ 61 mrad, respectively, based on a calibration elsewhere for the same instrument model [70].

Other general settings include a probe current of 4.3 pA and a convergence angle of 16 mrad. To minimize the effect of sample drifts during atomic-scale imaging, multiple rapidly scanned STEM images were recorded with a short dwell time of 2.4 µs/pixel for the same sample areas. These images were then cross-correlated in a post-processing step to reconstruct the final drift-corrected images having sufficient signal-to-noise ratios.

EELS-STEM was recorded in the DualEELS mode using a Gatan Quantum ER imaging filter. A collection angle of 35 mrad was used for the EELS spectrometer. Spectrum images were collected under a probe current of 32 pA and a dwell time of 0.25 s/pixel. Each spectrum of the line scan series was dose-averaged over a length of ~10 nm parallel to the LSM/YSZ interface, effectively minimizing the effect of beam-induced damage. In the post-processing steps, the integral intensities for O K, Mn $L_{3,2}$, and La $M_{5,4}$-edges were calculated by integrating the core-loss edge intensity over an energy window of 40 eV from the edge onset after subtracting the pre-edge background. The oxidation states of Mn were determined from the peak ratio of Mn L_3/L_2-edges relative to the bulk LSM reference far away from the LSM/YSZ interface. To reduce the effect of Gaussian and Poison noise in the spectra for the calculation of Mn L_3/L_2 ratios, addition processing with non-negative matrix factorization was also used [59, 60].

EDX-STEM was performed on a Talos F200X (ThermoFisher Scientific, USA) at 200 kV. The instrument was equipped with four silicon drift detectors in a Super-X design, allowing a total solid angle of 0.9 sr. Acquisition settings for EDX spectrum images include a dwell time of 25 μs/pixel and a probe current of 119 pA.

4.5 | Quantitative STEM Image Analysis

The workflow to extract the projected interatomic spacing and atomic displacements from the drift-corrected STEM images is as follows. First, selected atomic columns in the STEM images were fitted with two-dimensional (2D) Gaussian functions to identify their precise coordinates (x_i, y_i for a column i^{th}) using the open-source package StatSTEM [71]. Subsequent processing was performed using Python scripting to calculate the 2D distribution of the interatomic spacings *dx* and *dy* along the horizontal and vertical axes, respectively, over the original STEM images. For displacement analysis, a set of orthogonal reference axes ($\vec{x}_o$ and $\vec{y}_o$) was defined within the bulk LSM or YSZ regions. The magnitudes for $\vec{x}_o$ and $\vec{y}_o$ are based on the mean values from the histograms of previously computed *dx* and *dy*. These reference axes thus provide the basis for extending a set of artificial reference lattices ($x_{i,\mathrm{ref}}$, $y_{i,\mathrm{ref}}$) over the original STEM images via translational symmetry operation. Finally, the displacement vectors were calculated from the difference between the actual lattice positions (x_i, y_i) and the corresponding reference lattices ($x_{i,\mathrm{ref}}$, $y_{i,\mathrm{ref}}$).

4.6 | X-Ray Spectroscopy

All X-ray photoelectron spectroscopy (XPS) and XAS measurements in this study were performed at the innovative station for in situ spectroscopy (ISISS) beamline at BESSY II, electron storage ring operated by the Helmholtz–Zentrum Berlin für Materialien und Energie, Berlin. This advanced facility integrates a soft X-ray beamline with a near-ambient pressure X-ray photoelectron spectroscopy (NAP-XPS) and XAS setup. It allows for surface science experiments under UHV as well as in situ investigations of solid surface-gas interactions, accommodating gas pressures up to 10 mbar in its reaction chamber. The custom-built NAP setup hosts a a SPECS PHOIBOS 150 NAP

spectrometer. Further details of the setup and the soft X-ray beamline are available at the Helmholtz–Zentrum Berlin website.

The thin-film samples, coupled with a K-type thermocouple, were mounted on a sapphire sample holder sandwiched between two stainless steel plates. The front plate had a circular opening to facilitate sample irradiation by the X-ray beam and allow for emitted photoelectrons (XPS/XAS) measurements. This sapphire holder was subsequently inserted into the XPS reaction cell. For the ex situ annealed samples, measurements were conducted under UHV conditions at 10^{-8} mbar. In contrast, the in situ annealed sample was first measured under UHV before dosing a 0.5 mbar O_2 gas pressure into the reaction cell via a mass flow controller. The sample was then heated with a near-infrared laser (808 nm, 60 W max) directed at the back of the mounting plate, at a heating rate of 5°C/min until reaching 800°C. The initial (0 h) measurement was taken under these conditions, which were maintained at constant temperature and gas pressure for up to 24 h. The final measurements were performed before cooling the sample to room temperature at 5°C/min in the 0.5 mbar O_2 atmosphere.

XPS spectra of core-level regions (Sr 3d, Mn 2p, and La 3d) were recorded at kinetic energies of 150 and 950 eV. Valence band spectra were also collected for energy calibration relative to the Fermi edge. Data analysis and visualization were performed using Igor Pro software, which incorporated Shirley background correction for all XPS spectra. The AEY-XA spectra were normalized after a linear background correction, relative to the nonlattice oxide intensity signals.

4.7 | DFT

DFT [72, 73] calculations were performed using the electronic structure code CASTEP (Version 19.11) [74] with on-the-fly generated ultrasoft pseudopotentials and a plane wave basis cutoff of 900 eV. All DFT calculation employed a Monkhorst–Pack k-grid with a spacing of 0.05 1/ang [75]. The PBEsol exchange-correlation functional was used with a Hubbard U value of 5.0 eV on Mn, as determined in our previous work [5]. The cubic and rhombohedral LSM cells were taken from ICSD [54] at a nominal composition of $La_{0.83}Sr_{0.17}MnO_3$, corresponding to 5 La, 1 Sr, 6 Mn, and 18 O atoms. All computations were spin-polarized with Mn magnetic moments initialized to $\pm 4\ \mu$B, to obtain G-type antiferromagnetic configurations. The complete set of initialized spin configurations is provided in Table S1. Geometry optimization were performed using a Pulay mixing scheme in combination with the CASTEP BFGS variant [76]. To resolve subtle energy differences between spin states, the convergence tolerance for the free energy during geometry optimization was set to 1.0^{-5} eV/atom and the total energy convergence tolerance to 1.0^{-6} eV/atom. For both geometry optimization and (p)DOS computations, ionic positions and lattice parameters were constrained to follow the symmetry operations of the cell. For the (p)DOS, the total energy convergence tolerance was set to 1.0^{-6} eV/atom, the spectral eigenvalue convergence tolerance to 1.0^{-6} eV/atom and a spectral Monkhost-Pack kgrid spacing of 0.05 1/ang. The (p)DOS were generated using OPTADOS [77] with an adaptive broadening (adaptive smearing = 0.4, core broadening = True, Gaussian width = 0.5, Lorentzian width = 0.1, Lorentzian scale = 0.2).

4.8 | Classical Force Field Simulations

Bulk cells for lanthanum manganese oxide $LaMnO_3$ (LMO) and zirconium dioxide ZrO_2 were first obtained from the Inorganic Crystal Structure Database (ICSD) [54] and Materials Project database [78], respectively. From these bulk structures, the desired surface orientations LMO $[1{-}1{-}1]_{rh}$ and ZrO_2 $[110]_c$ were generated using the Python Materials Genomics (pymatgen) library [79]. The resulting surface cells were extended along the z-direction to create 100 Å supercells. LSM was modeled by introducing the same random Sr doping as in our DFT study $La_{0.83}Sr_{0.17}MnO_3$, while YSZ was constructed by introducing 8 mol% Y dopants together with a combination of aligned and randomly distributed oxygen vacancies to reflect experimental observations. The two halves were joined with an interfacial gap of 0.1 Å to form an interface with minimal in-plane lattice mismatch, using the slightly larger lattice constants to accommodate strain. A 15 Å vacuum was added on both sides of the interface. The combined supercells yield an overall stoichiometry of $La_{233}Sr_{47}Mn_{280}O_{1688}Zr_{368}Y_{64}$. About 30 random doping configurations were initialized and relaxed using a classical force field, combining parameters from [80] and [81] as described in [5] within LAMMPS [82] using a conjugate gradient optimizer. Full construction details and structural candidates are provided in the Supporting Information.

4.9 | Multislice Simulations of ABF Images

STEM image simulations were performed using the Dr.Probe software [83] with parameters matched to the experimental setup. Illumination settings included an effective geometric source radius (HWHM-Half Width at Half Maximum) of 0.04 nm, a radius of the illumination aperture of 16 mrad and an accelerating voltage of 200 kV. As detector angle for the ABF, 8 mrad $<\theta<$18 mrad was used in accordance with experiment. Input cells (thickness ≈20 nm) were extracted from the interface region of the force field relaxed models with automatic supercell discretization and equidistant slicing along the z-direction. For the frozen lattice configurations 100 variants per slice were generated, with thermal vibration parameters set to $Y^{3+} = Zr^{4+} = 1.9$, $Sr^{2+} = La^{3+} = 1.5$, $Mn^{3+} = 1.1$, and $O^{2-} = 3.3$. Image postprocessing was carried out using the OpenCV library [84–88].

Acknowledgments

The authors acknowledge discussion with Prof. Dr. Robert Schlögl and for granting access to the infrastructure of the AC department. This work was supported by the Deutsche Forschungsgemeinschaft (DFG, German Research Foundation) under the priority programme SPP 2080 DynaKat. F.P.S. and T.L. acknowledge support from the Federal Ministry of Education and Research in the framework of the project Catlab (03EW0015B). Moreover, this work was partially funded by the Deutsche Forschungsgemeinschaft (DFG, German Research Foundation) under Germany's Excellence Strategy– EXC2089/1–390776260. X.Q.T. and P.K. gratefully acknowledge the Deutsche Forschungsgemeinschaft (DFG) for funding this work in the framework of the Priority Program SPP 2080 "Catalysts and reactors under dynamic conditions for energy storage and conversion" under the grant number LU 2246/3-1. Additionally, X.Q.T. thanks Dr. T. Yamamoto (Kyushu University, Japan) for his support with the DigitalMicrograph script for drift-corrected STEM imaging. P.K. acknowledges Prof. Dr. Matt Probert for insightful discussions and

assistance with CASTEP. H.T. gratefully acknowledges funding by the Deutsche Forschungsgemeinschaft (DFG, German Research Foundation) as a Walter-Benjamin Fellow (project no. 534232519). The authors thank the Helmholtz-Zentrum Berlin für Materialien und Energie for the allocation of synchrotron radiation beamtime at ISISS (photons- 232-12583-IN/CO). All computations were performed on the high performance computer Raven and Viper of the Max Planck Computing & Data Facility. The authors thank the European Regional Development Fund and the State of Brandenburg for the Themis Z (3.1) microscope (part of the Potsdam Imaging and Spectral Analysis (PISA) facility). Grammar and Orthography was partially checked by the use of AI.

Open Access funding enabled and organized by Projekt DEAL.

Funding

This study was supported by the Deutsche Forschungsgemeinschaft (LU 2246/3-1) and Bundesministerium für Bildung und Forschung (03EW0015B).

Conflicts of Interest

The authors declare no conflicts of interest.

Data Availability Statement

The data that support the findings of this study are available at Edmond: Research Data related to the Publication "Interfacial Atomic and Electronic Structures Revealed by LSM/YSZ Thin Film Studies as Model for SOECs," https://doi.org/10.17617/3.8BE2FR.

References

1. Q. Hassan, A. K. Nassar, A. K. Al-Jiboory, et al., "Mapping Europe Renewable Energy Landscape: Insights into Solar, Wind, Hydro, and Green Hydrogen Production," *Technology in Society* 77 (2024): 102535.

2. A. Hauch, R. Küngas, P. Blennow, et al., "Recent Advances in Solid Oxide Cell Technology for Electrolysis," *Science* 370 (2020): eaba6118.

3. E. D. Wachsman and K. T. Lee, "Lowering the Temperature of Solid Oxide Fuel Cells," *Science* 334 (2011): 935.

4. S. R. Foit, I. C. Vinke, L. G. J. D. Haart, and R. Eichel, "Power-to-Syngas: An Enabling Technology for the Transition of the Energy System? Minireviews," *Angewandte Chemie International Edition* 56 (2017): 5488.

5. H. Türk, F.-P. Schmidt, T. Götsch, et al., "Complexions at the Electrolyte/Electrode Interface in Solid Oxide Cells," *Advanced Materials Interfaces* 8 (2021): 2100967.

6. H. Türk, T. Götsch, F.-P. Schmidt, et al., *ChemCatChem* 14 (2022): e202200300.

7. H. Türk, X. Q. Tran, P. König, et al., "Boon and Bane of Local Solid State Chemistry on the Performance of LSM-Based Solid Oxide Electrolysis Cells," *Advanced Energy Materials* 15 (2025): 2405599.

8. A. Ramirez, "Colossal Magnetoresistance," *Journal of Physics: Condensed Matter* 9 (1997): 8171.

9. K. A. Gschneidner, V. Pecharsky, and A. Tsokol, "Recent Developments in Magnetocaloric Materials, *Reports on Progress in Physics* 68 (2005): 1479.

10. S. P. Jiang, "Development of Lanthanum Strontium Manganite Perovskite Cathode Materials of Solid Oxide Fuel Cells: a Review," *Journal of Materials Science* 43 (2008): 6799.

11. K. Horiba, A. Chikamatsu, H. Kumigashira, et al., "In Vacuo PPhotoemissionstudy of Atomically Controlled $La_{1-x}Sr_xMnO_3$ Thin Films: Composition Dependence of the Electronic Structure," *Physical Review B—Condensed Matter and Materials Physics* 71 (2005): 155420.

12. A. M. Saranya, D. Pla, A. Morata, et al., "Engineering Mixed Ionic Electronic Conduction in $La_{0.8}Sr_{0.2}MnO_{3+\delta}$ Nanostructures through Fast Grain Boundary Oxygen Diffusivity," *Advanced Energy Materials* 5 (2015): 1500377.

13. E. Navickas, T. M. Huber, Y. Chen, et al., "Fast Oxygen Exchange and Diffusion Kinetics of Grain Boundaries in Sr-doped $LaMnO_3$ Thin Films," *Physical Chemistry Chemical Physics* 17 (2015): 7659.

14. F. Chiabrera, I. Garbayo, L. López-Conesa, et al., "Engineering Transport in Manganites by Tuning Local Nonstoichiometry in Grain Boundaries," *Advanced Materials* 31 (2019): 1805360.

15. K. Navin and R. Kurchania, "The Effect of Particle Size on Structural, Magnetic and Transport Properties of $La_{0.7}Sr_{0.3}MnO_3$ Nanoparticles," *Ceramics International* 44 (2018): 4973.

16. Z. Liao, M. Huijben, Z. Zhong, et al., "Controlled lateral Anisotropy in Correlated Manganite Heterostructures by Interface-engineered Oxygen Octahedral Coupling," *Nature Materials* 15 (2016): 425.

17. Y. Zhu, X. Ma, M. Zhang, et al., "Structure and Microstructural Characteristics in the Thin Films of $La_{1-x}Sr_xMnO_3$ (x = 0.1, 0.2, 0.3)," *Materials Letters* 58 (2004): 1485.

18. S. Mandal, A. K. Gupta, B. H. Beavers, V. Singh, J. Narayan, and R. Sachan, "Atomic-scale Insights on Large-misfit Heterointerfaces in LSMO/MgO/c-Al_2O_3," *Crystals* 11 (2021): 1493.

19. P. Rajak, D. Knez, S. K. Chaluvadi, et al., "Evidence of Mn-ion Structural Displacements Correlated with Oxygen Vacancies in $La_{0.7}Sr_{0.3}MnO_3$ Interfacial Dead Layers," *ACS Applied Materials & Interfaces* 13 (2021): 55666.

20. J. Fleig, F. Baumann, V. Brichzin, et al., "Thin Film Microelectrodes in SOFC Electrode Research," *Fuel Cells* 6 (2006): 284.

21. J. Fleig, H.-R. Kim, J. Jamnik, and J. Maier, "Oxygen Reduction Kinetics of Lanthanum Manganite (LSM) Model Cathodes: Partial Pressure Dependence and Rate-Limiting Steps," *Fuel Cells* 8 (2008): 330.

22. L. Yan, K. Balasubramaniam, S. Wang, H. Du, and P. A. Salvador, "Effects of Crystallographic Orientation on the Oxygen Exchange Rate of $La_{0.7}Sr_{0.3}MnO_3$ Thin Films," *Solid State Ionics* 194 (2011): 9.

23. T. Huber, M. Kubicek, A. Opitz, and J. Fleig, "The Relevance of Different Oxygen Reduction Pathways of $La_{0.8}Sr_{0.2}MnO_3$ (LSM) Thin Film Model Electrodes," *Journal of the Electrochemical Society* 162 (2014): F229.

24. L. Zhang, S. Wang, H. Huang, Y. Li, Y. Lu, and C. Xia, "Promotion Effect of Metal Nanoparticle on Surface Exchange Reaction of (La, Sr) MnO_3 Film with Different Orientation," *Journal of the Electrochemical Society* 164 (2017): F610.

25. W. Hizi, H. Rahmouni, K. Khirouni, and E. Dhahri, "Consistency between Theoretical Conduction Models and Experimental Conductivity Measurements of Strontium-doped Lanthanum Manganite," *Journal of Alloys and Compounds* 957 (2023): 170418.

26. F. W. Poulsen, "Defect Chemistry Modelling of Oxygen-stoichiometry, Vacancy Concentrations, and Conductivity of $(La_{1-x}Sr_x)_yMnO_{3\pm\delta}$," *Solid State Ionics* 129 (2000): 145.

27. S. Piskunov, E. Spohr, T. Jacob, E. A. Kotomin, and D. E. Ellis, "Electronic and Magnetic Structure of $La_{0.875}Sr_{0.125}MnO_3$ calculated by Means of Hybrid Density-Tunctional Theory," *Physical Review B—Condensed Matter and Materials Physics* 76 (2007): 012410.

28. M. Pavone, A. B. Munoz-Garcia, A. M. Ritzmann, and E. A. Carter, "First-principles Study of Lanthanum Strontium Manganite: Insights into Electronic Structure and Oxygen Vacancy Formation," *The Journal of Physical Chemistry C* 118 (2014): 13346.

29. Y. Sun, X. Xu, and Y. Zhang, "Variable-range Hopping of Small Polarons in Mixed-valencemanganites," *Journal of Physics: Condensed Matter* 12 (2000): 10475.

30. L. Yan and P. A. Salvador, "Substrate and Thickness Effects on the Oxygen Surface Exchange of $La_{0.7}Sr_{0.3}MnO_3$ Thin Films," *ACS Applied Materials & Interfaces* 4 (2012): 2541.

31. E. Navickas, Y. Chen, Q. Lu, et al., "Dislocations Accelerate Oxygen Ion Diffusion in $La_{0.8}Sr_{0.2}MnO_3$ Epitaxial Thin Films," *ACS Nano* 11 (2017): 11475.

32. M. Ni, M. K. Leung, and D. Y. Leung, "Technological Development of Hydrogen Production by Solid Oxide Electrolyzer Cell (SOEC)," *International Journal of Hydrogen Energy* 33 (2008): 2337.

33. T. T. Fister, D. D. Fong, J. A. Eastman, et al., "In Situ Characterization of Strontium Surface Segregation in Epitaxial $La_{0.7}Sr_{0.3}MnO_3$ Thin Films as a Function of Oxygen Partial Pressure," *Applied Physics Letters* 93 (2008): 15.

34. H. Jalili, Y. Chen, and B. Yildiz, "Structural, Chemical, and Electronic State on $La_{0.7}Sr_{0.3}MnO_3$ Dense Thin-film Surfaces at High Temperature: Surface Segregation," *ECS Transactions* 28 (2010): 235.

35. A. Mitterdorfer and L. Gauckler, "$La_2Zr_2O_7$ Formation and Oxygen Reduction Kinetics of the $La_{0.85}Sr_{0.15}Mn_yO_3$, $O_2(g)$| YSZ System," *Solid State Ionics* 111 (1998): 185.

36. Y. Chen, L. Yang, F. Ren, and K. An, "Visualizing the Structural Evolution of LSM/xYSZ Composite Cathodes for SOFC by in-situ Neutron Diffraction," *Scientific Reports* 4 (2014): 5179.

37. A. Abdelaziem, K. El-Khatib, M. Hafez, and Y. Badr, Effect of Annealing on $La_{0.8}Sr_{0.2}MnO_3$ Thin Films Prepared by Pulsed Laser Deposition, *Spectrochimica Acta Part A: Molecular and Biomolecular Spectroscopy* 211 (2019): 100.

38. A. J. Darbandi, T. Enz, and H. Hahn, "Synthesis and Characterization of Nanoparticulate Films for Intermediate Temperature Solid Oxide Fuel Cells," *Solid State Ionics* 180 (2009): 424.

39. M. P. Seah and W. Dench, "Quantitative Electron Spectroscopy of Surfaces: A Standard Data Base for Electron Inelastic Mean Free Paths in Solids," *Surface and Interface Analysis* 1 (1979): 2.

40. V. Vibhu, I. C. Vinke, R.-A. Eichel, and L. de Haart, "$La_{0.6}Sr_{0.4}MnO_3$-based Fuel Electrode Materials for Solid Oxide Electrolysis Cells Operating under Steam, CO_2, and Co-electrolysis Conditions," *Energies* 16 (2023): 7115.

41. J. Labrincha, J. Frade, and F. Marques, "$La_2Zr_2O_7$ formed at Ceramic Electrode/YSZ Contacts," *Journal of Materials Science* 28 (1993): 3809.

42. X. Liu, J. Che, H. Yi, J. Zhang, and G. Liang, "Diffusion Mechanism of Oxygen Ions in $La_2Zr_2O_7$/YSZ Composite Ceramics," *Journal of Alloys and Compounds* 778 (2019): 522.

43. C. V. Thompson, "Solid-state Dewetting of Thin Films," *Annual Review of Materials Research* 42 (2012): 399.

44. F. Leroy, F. Cheynis, Y. Almadori, et al., "How to Control Solid State Dewetting: A Short Review *Surface Science Reports* 71 (2016): 391.

45. B. Cui, C. Song, F. Li, et al., "Tuning the Entanglement between Orbital Reconstruction and Charge Transfer at a Film Surface," *Scientific Reports* 4 (2014): 4206.

46. D. Vlachos, A. Craven, and D. McComb, "The Influence of Dopant Concentration on the Oxygen K-edge ELNES and XANES in Yttria-stabilized Zirconia," *Journal of Physics: Condensed Matter* 13 (2001): 10799.

47. P. Jacquet, R. Podor, J. Ravaux, et al.,"On the Solid-state Dewetting of Polycrystalline Thin Films: Capillary Versus Grain Growth Approach," *Acta Materialia* 143 (2018): 281.

48. N. Andreas, R. Christoph, R. Raffael, et al., "Ambient Pressure XPS Study of Mixed Conducting Perovskite-type SOFC Cathode and Anode Materials under Well-defined Electrochemical Polarization," *The Journal of Physical Chemistry C* 120 (2016): 1461.

49. J. Kuo, H. U. Anderson, and D. M. Sparlin, "Oxidation-reduction Behavior of Undoped and Sr-doped $LaMnO_3$: Defect Structure, Electrical Conductivity, and Thermoelectric Power," *Journal of Solid State Chemistry* 87 (1990): 55.

50. H. Yokokawa, N. Sakai, T. Kawada, and M. Dokiya, "Thermodynamic Analysis on Interface between Perovskite Electrode and YSZ Electrolyte," *Solid State Ionics* 40 (1990): 398.

51. R. Knibbe, A. Hauch, J. Hjelm, S. D. Ebbesen, and M. Mogensen, "Durability of Solid Oxide Cells," *Green* 1 (2011): 141.

52. O. Chmaissem, B. Dabrowski, S. Kolesnik, J. Mais, J. Jorgensen, and S. Short, "Structural and Magnetic Phase Diagrams of $La_{1-x}Sr_xMnO_3$ and $Pr_{1-y}Sr_yMnO_3$," *Physical Review B* 67 (2003): 094431.

53. C. Ma, Z. Yang, and S. Picozzi, "Ab Initio Electronic and Magnetic Structure in $La_{0.66}Sr_{0.33}MnO_3$: Strain and Correlation Effects," *Journal of Physics: Condensed Matter* 18 (2006): 7717.

54. D. Zagorac, H. Müller, S. Ruehl, J. Zagorac, and S. Rehme, "Recent Developments in the Inorganic crystal Structure Database: Theoretical Crystal Structure Data and Related Features," *Journal of Applied Crystallography* 52 (2019): 918.

55. T. Okugawa, K. Ohno, Y. Noda, and S. Nakamura, "Weakly Spin-dependent Band Structures of Antiferromagnetic Perovskite $LaMO_3$ (M = Cr, Mn, Fe)," *Journal of Physics: Condensed Matter* 30 (2018): 075502.

56. Z. Li, D. Song, R. Yu, et al., "Competing Interfacial Reconstruction Mechanisms in $La_{0.7}Sr_{0.3}MnO_3/SrTiO_3$ Heterostructures," *ACS Applied Materials & Interfaces* 8 (2016): 24192.

57. H. Guo, Z. Wang, S. Dong, et al., "Interface-induced Multiferroism by Design in Complex Oxide Superlattices," *Proceedings of the National Academy of Sciences* 114 (2017): E5062.

58. A. Bhargava, R. Eppstein, J. Sun, et al., "Breakdown of the Small-polaron Hopping Model in Higher-order Sapinels," *Advanced Materials* 32 (2020): 2004490.

59. M. Shiga, K. Tatsumi, S. Muto, et al., "Sparse Modeling of EELS and EDX Spectral Imaging Data by Nonnegative Matrix Factorization," *Ultramicroscopy* 170 (2016): 43.

60. M. Shiga and S. Muto, "Non-negative Matrix Factorization and its Extensions for Spectral Image Data Analysis," *E-Journal of Surface Science and Nanotechnology* 17 (2019): 148.

61. Y.-M. Kim, A. Morozovska, E. Eliseev, et al., "Direct Observation of Ferroelectric Field Effect and Vacancy-controlled Screening at the $BiFeO_3/La_xSr_{1-x}MnO_3$ Interface," *Nature Materials* 13 (2014): 1019.

62. D. Rasic, R. Sachan, J. Prater, and J. Narayan, "Structure-property Correlations in Thermally Processed Epitaxial LSMO Films," *Acta Materialia* 163 (2019): 189.

63. F. Yang, S. Kim, and Y. Takamura, "Strain Effect on the Electrical Conductivity of Epitaxial $La_{0.67}Sr_{0.33}MnO_3$ Thin Films," *Scripta Materialia* 65 (2011): 29.

64. A. Lussier, J. Dvorak, S. Stadler, et al., "Stress Relaxation of $La_{1/2}Sr_{1/2}MnO_3$ and $La_{2/3}Ca_{1/3}MnO_3$ at Solid Oxide Fuel Cell Interfaces," *Thin Solid Films* 516 (2008): 880.

65. M. Siebenhofer, U. Haselmann, A. Nenning, et al., "Surface Chemistry and Degradation Processes of Dense $La_{0.6}Sr_{0.4}CoO_{3-\delta}$ Thin Film Electrodes," *Journal of the Electrochemical Society* 170 (2023): 014501.

66. J. M. Börgers, J. Kler, K. Ran, et al., "Faster Diffusion of Oxygen along Dislocations in $(La,Sr)MnO_{3+\delta}$ is a Space-charge Phenomenon," *Advanced Functional Materials* 31 (2021): 2105647.

67. E. Okunishi, I. Ishikawa, H. Sawada, F. Hosokawa, M. Hori, and Y. Kondo, "Visualization of Light Elements at Ultrahigh Resolution by STEM Annular Bright Field Microscopy," *Microscopy and Microanalysis : the Official Journal of Microscopy Society of America, Microbeam Analysis Society, Microscopical Society of Canada* 15 (2009): 164.

68. T. Lunkenbein, F. Girgsdies, A. Wernbacher, et al., "Direct Imaging of Octahedral Distortion in a Complex Molybdenum Vanadium Mixed Oxide," *Angewandte Chemie* 127 (2015): 6932.

69. R. Ishikawa, E. Okunishi, H. Sawada, Y. Kondo, F. Hosokawa, and E. Abe, "Direct Imaging of Hydrogen-atom Columns in a Crystal by Annular Bright-field Electron Microscopy," *Nature Materials* 10 (2011): 278.

70. L. Jones, A. Varambhia, H. Sawada, and P. Nellist, "An Optical Configuration for Fastidious STEM Detector Calibration and the Effect of the Objective-lens Pre-field," *Journal of Microscopy* 270 (2018): 176.

71. A. De Backer, K. Van den Bos, W. Van den Broek, J. Sijbers, and S. Van Aert, "StatSTEM: An Efficient Approach for Accurate and Precise Model-based Quantification of Atomic Resolution Electron Microscopy Images," *Ultramicroscopy* 171 (2016): 104.

72. P. Hohenberg and W. Kohn, "Inhomogeneous Electron Gas," *The Physical Review* 136 (1964): B864.

73. W. Kohn and L. J. Sham, "Self-consistent Equations including Exchange and Correlation Effects," *The Physical Review* 140 (1965): A1133.

74. S. J. Clark, M. D. Segall, C. J. Pickard, et al., "First Principles Methods using CASTEP," *Zeitschrift für Kristallographie* 220 (2005): 567.

75. H. J. Monkhorst and J. D. Pack, "Special Points for Brillouin-zone Integrations," *Physical Review B* 13 (1976): 5188.

76. B. G. Pfrommer, M. Cote, S. G. Louie, and M. L. Cohen, "Relaxation of Crystals with the Quasi-Newton Method," *Journal of Computational Physics* 131 (1997): 233.

77. R. J. Nicholls, A. J. Morris, C. J. Pickard, and J. R. Yates, "OptaDOS-a New Tool for EELS Calculations," *Journal of Physics. Conference Series* 371 (2012): 2.

78. M. K. Horton, P. Huck, R. X. Yang, et al., "Accelerated Data-driven Materials science with the Materials Project," *Nature Materials* 24 (2025): 1532.

79. S. P. Ong, W. D. Richards, A. Jain, et al., "Python Materials Genomics (pymatgen): A Robust, Open-source Python Library for Materials Analysis," *Computational Materials Science* 68 (2013): 314.

80. H. W. Brinkman, "Molecular Dynamics Simulations of Yttria-stabilized Zirconia," *Chemical Physics Letters* 247 (1995): 386.

81. M. S. Islam, M. Cherry, and C. R. A. Catlow, "Oxygen Diffusion in $LaMnO_3$ and $LaCoO_3$ Perovskite-type Oxides: A Molecular Dynamics Study," *Journal of Solid State Chemistry* 124 (1996): 230.

82. A. P. Thompson, H. M. Aktulga, R. Berger, et al., "LAMMPS-a Flexible Simulation Tool for Particle-based Materials Modeling at the Atomic, Meso, and Continuum Scales," *Computer Physics Communications* 271 (2022): 108171.

83. J. Barthel, "Dr. Probe: A Software for High-resolution STEM Image Simulation," *Ultramicroscopy* 193 (2018): 1.

84. G. Bradski, "The Opencv Library," *Dr. Dobb's Journal:Software Tools for the Professional Programmer* 25 (2000) 123.

85. C. Scheurer, Research Data Related to the Publication Interfacial Atomic and Electronic Structures Revealed by LSM/YSZ Thin Film Studies as Model for SOECs, (Edmond, 2025), https://doi.org/10.17617/3.8BE2FR.

86. FHI-aims Team, FHI-aims: All-Electron Electronic Structure Theory with Numeric Atom-Centered Basis Functions—A Users' Guide, Fritz Haber Institute (FHI) and Molecular Simulations from First Principles (MS1P), accessed: 2025-06-30.

87. Z. A. Piskulich, O. O. Mesele, and W. H. Thompson, "Activation Energies and Beyond," *The Journal of Physical Chemistry A* 123 (2019): 7185.

88. S. Fabris, A. T. Paxton, and M. W. Finnis, "A Stabilization Mechanism of Zirconia based on Oxygen Vacancies Only," *Acta Materialia* 50 (2002): 5171.

Supporting Information

Additional supporting information can be found online in the Supporting Information section. **Supporting Fig. S1:** EDX maps of the pristine LSM-5 film. HAADF-STEM image and corresponding EDX maps from an electron transparent lamella cut out from the LSM-5 film on an YSZ substrate. The elemental maps correspond to La L, Mn K, Sr K, Zr K and Y K lines. **Supporting Fig. S2:** EDX maps of the pristine LSM-200 film. HAADF-STEM image and corresponding EDX maps from an electron transparent lamella cut out from the LSM-200 film on an YSZ substrate. The elemental maps correspond to La L, Mn K, Sr K, Zr K and Y K lines. **Supporting Fig. S3:** EDX maps of the LSM-5 film after annealing at 1150°C in air for 1 hr. HAADF-STEM image and corresponding EDX maps from an electron transparent lamella cut out from the LSM-5 film on an YSZ substrate. The elemental maps correspond to La L, Mn K, Sr K, Zr K and Y K lines. Significant phase separation can be seen in the post-annealed film. **Supporting Fig. S4:** EDX maps of the LSM-200 film after annealing at 1150°C in air for 1 hr. HAADF-STEM image and corresponding EDX maps from an electron transparent lamella cut out from the LSM-200 film on an YSZ substrate. The elemental maps correspond to La L, Mn K, Sr K, Zr K and Y K lines. The film generally remained homogeneous in elemental distribution of La, Sr and Mn, despite some minor islands of the lanthanum zirconate (LZO). **Supporting Fig. S5:** Difference between the O K edge X-ray absorption spectra of the pristine sample and the 12 h annealed sample. The difference between the X-ray absorption spectra of the pristine sample (black) and the 12 h annealed sample (red) is displayed as the yellow trace. For comparison, a reference O K-edge spectrum of 10 mol% YSZ,is adapted from the literature [46]. The similarity between the difference spectrum and the YSZ reference indicates that the apparent increase in X-ray absorption intensity after 12 h annealing originates from the substrate, consistent with the dewetting of the LSM film. **Supporting Fig. S6:** X-ray photoelectron spectroscopy (XPS) spectra of the Sr 3d, Mn 2p, and La 3d core levels for the LSM-5 thin film in its pristine state, and after ex-situ annealing in air at 800°C for 1 hour and 12 hours. The measurements were performed using photon energies selected to yield kinetic energies of 150 eV and 950 eV, providing surface- and subsurface-sensitive information, respectively. The consistent spectral features across all annealing durations indicate that the chemical composition and electronic structure of the LSM-5 film remain stable during thermal treatment under atmospheric conditions. **Supporting Fig. S7:** O K-edge and Mn L-edges XA spectra recorded for the in-situ annealed LSM-5 film at 800°C in 0.5 mbar O_2 atmosphere at 0, 12, and 24 hours. Both the O K-edge XAS (left panel) and the Mn L-edges XAS (right panel) show no significant changes in the XA signal with increasing annealing duration in the XPS reaction cell. This indicates a stable morphology of the thin film under these reduced oxygen pressure conditions, in contradict to the ex-situ annealed sample in air discussed in the main text. Notably, the O K-edge spectra of the in-situ sample show higher substrate XA-signals contributions from YSZ compared to the ex-situ annealed sample due to its enhanced electronic conductivity at elevated temperature. In addition, the oxygen background in the reaction cell suppresses the XA intensity at 531 eV, which corresponds to the π^* resonance of molecular oxygen. **Supporting Fig. S8:** Sr 3d, Mn 2p, and La 3d core-level X-ray photoelectron spectra (XPS) were recorded during the in-situ annealed of the LSM-5 film at 800°C in a 0.5 mbar O_2 atmosphere over a duration of 24 hours (0, 6, 12, 18, and 24 hours). The spectra were collected at two different kinetic energies, 150 eV and 950 eV, corresponding to surface-sensitive and subsurface-sensitive measurements, respectively. Left Panel (Sr 3d): all the Sr 3d core-level spectra present XPS contribution from the surface Sr as well as the Sr bulk species, however their ratio differs depending on the probing depth(kinetic energy). The one measured at 150 eV (top tier) reveal photoelectron signals primarily dominating from surface Sr species, as this kinetic energy corresponds to a shorter inelastic mean free path of electrons. Conversely, the spectra recorded at 950 eV (bottom tier) are more bulk-sensitive, capturing contributions from Sr species within

the thin film matrix. The doublet feature of Sr 3d remains consistent, highlighting the interaction of surface species with the O_2 atmosphere, as well as the stability of bulk Sr species under the annealing conditions. A detailed fitting of the Sr 3d XPS spectra is presented in Figure S9 in this section. Middle Panel (Mn 2p): The Mn 2p spectra illustrate the oxidation state of Mn and its electronic environment. Signals recorded at 150 eV predominantly represent surface species, while those at 950 eV reveal contributions from the bulk of the thin film. No significant changes are observed, indicating that the Mn-containing phases maintain their chemical stability throughout the annealing process. Right Panel (La 3d): The La 3d spectra display the characteristic doublet structure corresponding to La species within the LSM thin film as well as their satellites peaks. Similar to the Sr and Mn spectra, the top-tier measurements at 150 eV probe more surface species, while the bottom tier at 950 eV is dominated by bulk contributions. The spectra confirm the preservation of La oxidation state during annealing. Across all panels, the XPS measurements demonstrate that the elemental composition and chemical environment of Sr, Mn, and La within the LSM thin film as well as at its surface remain stable throughout the 24-hour in-situ annealing process at 800°C in 0.5 mbar O_2. This stability underscores the robustness of the thin film under high-temperature and low-oxygen pressure conditions, and its compatibility for future potential of operando XPS examination of thin film LSM electrode-SOC under electrochemical operating conditions. **Supporting Fig. S9:** Fitting of the Strontium 3d X-ray photoelectron spectra of the pristine LSM-5 thin film, acquired at photoelectron kinetic energies of 150 eV (left panel) and 950 eV (right panel), corresponding to surface- and subsurface-sensitive measurements, respectively. The fitting procedure follows the same protocol adapted from References[6,48]. Each spectrum is deconvoluted into four components: two peaks attributed to surface Sr species (shown in red) and two to bulk Sr species (shown in gray). As anticipated, the 150 eV spectrum exhibits a dominant surface Sr contribution, while the 950 eV spectrum shows a greater relative contribution from bulk Sr, reflecting the increased probing depth. **Supporting Fig. S10:** Effect of annealing (1150°C, air, 1 hr) on the LSM-200 film. (a,b) Top-view secondary electron SEM micrographs of the LSM-200 film on an YSZ substrate for the pristine and annealed samples, respectively. (c,d) Cross-sectional view BF-STEM images of the LSM/YSZ interfaces for the pristine and annealed samples, respectively. Nanoscale islands of the $La_2Zr_2O_7$ (LZO) pyrochlore phase were observed in the annealed film. **Supporting Fig. S11:** Evidence of the $La_2Zr_2O_7$ (LZO) pyrochlore in the annealed LSM-200 film (1150°C, air, 1 hr). (a) Survey BF-STEM image and corresponding EDX maps of the LSM/YSZ interface. The elemental maps correspond to La L, Mn K, Sr K, Zr K and Y K lines. (b) High-resolution BF-STEM image of an LZO island at the LSM/YSZ interface, which is confirmed by its characteristic superspots in the corresponding FFT. **Supporting Fig. S12:** EDX maps of the LSM-5 film after annealing at 800°C for 6 days. HAADF-STEM image and corresponding EDX maps from an electron transparent lamella cut out from the 5 nm LSM film on an YSZ substrate. The elemental maps correspond to La L, Mn K, Sr K, Zr K and Y K lines. **Supporting Fig. S13:** Lattice mismatch between LSM and YSZ. (a) LAADF-STEM image of the LSM/YSZ interface in a pristine 30 nm film viewed along the LSM $[241]_{rh}$ || YSZ $[001]_c$ orientations. (b) Overlaid fast Fourier transforms (FFTs) of the LSM and YSZ regions in (a). (c) Estimated mismatch of the corresponding lattice planes between LSM and YSZ. **Supporting Fig. S14:** Variants of the interfacial orientations between LSM and YSZ. (a-c) Given the same orientation of the YSZ substrate, several crystal orientations of the LSM domains arise in the PLD-grown films, exemplified for a film with a thickness of 30 nm. Imaging was performed in the low-angle annular dark-field (LAADF-STEM) mode. Note that the orientation in (a) is the most frequently found one. **Supporting Fig. S15:** An interface between LSM and YSZ in the LSM-200 sample. High-angle annular dark-field (HAADF-STEM) image of the LSM/YSZ interface in the LSM-200 sample after annealing at 1150°C in air for 1 hr. The measurement was performed on the Themis Z (3.1) (ThermoFisher Scientific, USA) at 300 kV. **Supporting Fig. S16:** Structures for the spin-dependent pDOS computations and energy distribution of the full spin configurational space after relaxation. a) Cubic $La_{0.83}Sr_{0.17}MnO_3$ unit cell containing the non-rotated MnO_6 octahedral motif. The numbers on the Mn atoms correspond to the enumeration from Table S1 for the AFM spin states. b) Rhombohedral $La_{0.83}Sr_{0.17}MnO_3$ unit cell containing the rotated MnO_6 octahedral motif. The numbers on the Mn atoms correspond to the enumeration from Table S1 for the AFM spin states. c) After relaxing the initial spin states from Table S1 and coordinates of the cubic and rhombohedral unit cells, their energy distribution is plotted. The numbers (1), (2), and (3) represent each the most unstable, a metastable and the most stable relaxed structure for both, the cubic and the rhombohedral cell. The thermal energy range of 0.069 eV/atom, representing 800 K is included as a black bar. This shows that the full range of MnO_6 distortions is accessible during thin film synthesis and under operating conditions. **Supporting Fig. S17:** Relaxed geometries with highlighted MnO_6 octahedra for an unstable (1), metastable (2), and stable (3) AFM spin configurations (from Table S1) for the rhombohedral and cubic unit cell. a) The relaxed geometries of spin configurations AFM 1 (1), AFM 6 (2), and AFM 18 (3) as unstable (1), metastable (2), and stable (3) structures from energy diagram in Figure S16c. Stronger distortions in the MnO_6 octahedra can be seen, the more stable the structure becomes. b) The relaxed geometries of spin configurations AFM 6 (1), AFM 18 (2), and AFM 14 (3) as unstable (1), metastable (2), and stable (3) structures from energy diagram in Figure S16c. The non-rotated MnO_6 octahedra elongate more evenly in space upon relaxation than their rotated counterparts in the rhombohedral cell. **Supporting Fig. S18:** Visualization of changes upon relaxation with different initial spin configurations for one exemplary MnO_6 octahedron in the rhombohedral and cubic unit cell. The dashed lines show the inner connections of the oxygens forming the MnO_6 units. The solid lines represent the outer edges of the MnO6 octaehedra. a) The exemplary MnO_6 shows the representative trend that the oxygen positions deviate stronger (represented in different blue colors) from the non-relaxed octahedron motif (in black) for the rhombohedral unit cell. b) Analogously, one exemplary MnO_6 octahedron for the cubic unit cell, only that structure (1), (2), and (3) correspond to AFM 6, 18, and 14 respectively. The octahedral motif for the non-rotated alignment does not distort as much as for the rotated case. **Supporting Fig. S19:** Spin densities of the Mn d-orbitals and pDOS for the unstable (1), metastable (2), and stable (3) spin configuration for the rhombohedral unit cells with the rotated MnO_6 octahedron motif. Slight asymmetries in the spin distributions are visible which are reflected in the asymmetric difference of the spin up and spin down channels in the pDOS. For more stable structures, a more symmetric spin density and pDOS is obtained. a) Spin density and pDOS of the unstable structure (1) with AFM 1 spin arrangement (see Table S1). The intensites of the spin up and spin down densities show asymmetric values, leading to different pDOS spin up and down states around the Fermi level. Notably here is the difference between Mn 1, 3, and 5 in the spin-up channels for d-orbital 1 and 2 vs. their counterpart densities in Mn 2, 4, and 6 in the spin-down channels. b) Spin density and pDOS of a metastable structure (2) with AFM 6 spin arrangement. The biggest difference in spin density here is between Mn 1, 5, and 6 in the spin-up channels for d-orbital 1 and 2 vs. their counterpart densities in Mn 2, 3, and 4 in the spin-down channels. c) Spin density and pDOS of a stable structure (3) with AFM 18 spin arrangement. The difference between the spin up and spin down channels of the Mn d-orbitals is minute and mostly symmetric which is reflected in symmetric states of the pDOS around the Fermi level. **Supporting Fig. S20:** Spin densities of the Mn d-orbitals and pDOS for the unstable (1), metastable (2), and stable (3) spin configuration for the cubic unit cells with the non-rotated MnO_6 octahedron motif. The spin densities only show minute differences in the spin up and spin down channels which is reflected in symmetric behavior of the spin up and down channels in the pDOS, especially around the Fermi level. All cubic structures lead to continuous states. a) Spin density and pDOS of the unstable structure (1) with AFM 6 spin arrangement (see Table S1). b) Spin density and pDOS of the unstable structure (2) with AFM 18 spin arrangement. c) Spin density and pDOS of the unstable structure (3) with AFM 14 spin arrangement. **Supporting Fig. S21:** Construction of an atomistic model for the LSM/YSZ Interface. a) $[1\text{-}1\text{-}1]_{rh}$ LMO unit cell as starting point for the LSM interface half. b) $[110]_c$ ZrO_2 unit cell as starting point for the YSZ interface half. c) Combined interface. The LMO unit cell was cut into pseudocubic form, extended in z to a bulk-like interface cell, and doping with a nominal composition as in our bulk LSM DFT study

$La_{0.83}Sr_{0.17}MnO_3$ was introduced. The ZrO_2 supercell is created from the ZrO_2 model in b and yttrium dopants are introduced to match our experimental 8 mol% YSZ composition. The red arrow show row defects in the oxygen vacancy lattice in our initial guess. The rest of the oxygen vacancies are randomly distributed in the YSZ half. d) One example structure for a force field relaxed interface model. **Supporting Fig. S22:** Relaxation trajectory of zoomed in interface region. a) Initial structure. b) Initial lattice expansion driven by Coulomb repulsion from the combined lattices and by the introduced dopants and vacancies. c) Beginning of the atomic rearrangement on both sides of the interface. d) Coulomb attraction of the new lattice sites draws the atoms nearer, resulting in the contraction of the lattice. e) Interfacial gap is closed and atoms rearrange more strongly directly at the first two to three layers near the interface. f) Final structure of the relaxation trajectory. Suppressed MnO_6 rotation on the LSM side and disorder on the YSZ side. **Supporting Fig. S23:** The same interface halves relaxed for different gap distances. a) At an initial gap of −0.5 Å minimal atomic reorganization occurs on both sides of the interface. b) With an initial gap ofrotation. c) At an initial gap of 0.0 Å, stronger atomic rearrangements occur on both sides, with reduced MnO−0.1 Å, atoms rearrange more noticeably, initiating suppression of the MnO rotations in the first LSM_6 layer near the interface. d) For an initial gap of 0.1 Å, the MnO_6 octahedrons are in non-rotated arrangement in the first layer of the LSM side, while the YSZ side shows enhanced reorganization including defect formation. e) At an initial gap of 0.5 Å, the suppression of MnO_6 rotations extends into the first two layers of the LSM side and the YSZ side exhibits more extensive reorganization with larger voids and defect states. f) For an initial gap of 1.0 Å, the suppression of the rotation of the MnO_6 octahedrons persists into the first two layers of the LSM side and the YSZ side undergoes severe reordering, resulting in an almost disconnected interface dominated by voids. **Supporting Fig. S24:** Different relaxed interfacial models and their corresponding simulated ABF-STEM images. While all interfaces exhibit the suppressed MnO_6 rotation at the interface, the atomic reorganization and formation of voids on the YSZ side is governed by the specific arrangement of the yttrium dopants. **Supporting Table S1:** Table of full spin configurational space for all Mn atoms in the for the cubic and rhombohedral cell. The number of the Mn atoms corresponds to the enumeration in Figure S16a for the cubic and Figure S16b for the rhombohedral unit cell.